Iranian Journal of Mathematical Chemistry

IJMC

DOI: 10.22052/IJMC.2025.257706.2074
Vol. 17, No. 2, 2026, pp. 137-177
Research Paper

Extended Fractional-Time Oregonator Model Accounting for Proton Dynamics

Sarita Pippal[1*]

[1]Department of Mathematics, Panjab University, Chandigarh, India.

Keywords:
Chemical reaction kinetics,
Fractional-order dynamical system,
Nullcline analysis,
Local stability analysis

AMS Subject Classification (2020):

334A08; 34D20; 34C23; 34C60

Article History:

Received: 4 October 2025
Accepted: 3 December 2025

Abstract

In this manuscript, we develop a generalized form of the classical three–variable Oregonator model by extending it to a four–dimensional fractional–order system. The extended formulation explicitly includes the proton concentration $\mathcal{H}(t)$ within the Belousov–Zhabotinsky (BZ) reaction kinetics and introduces memory effects through the Caputo fractional derivative of order $\alpha \in (0, 1]$. For the classical case $\alpha = 1$, the model reduces to an ordinary differential equation system, which is solved using the third–order Adams–Bashforth–Moulton (ABM3) predictor–corrector method and compared with the standard fourth–order Runge–Kutta (RK4) scheme. For $0 < \alpha < 1$, the system is numerically integrated using the fractional ABM3 method, where the Caputo derivative is discretized by means of convolution–type memory weights.

Numerical experiments reveal that both proton feedback plays a crucial role in shaping the oscillatory dynamics and stabilizing the long–term behavior. Analytical results further confirm positivity and boundedness of the solutions, characterize the equilibrium points, and determine their stability. The trivial equilibrium is always unstable, whereas the nontrivial equilibrium is locally asymptotically stable under realistic parameter conditions. Sensitivity and eigenvalue analysis additionally show that the parameters (a, q) tend to destabilize the system, while $(\delta, \varepsilon, \gamma)$ enhance stability. Here, a and q represent the autocatalytic and inhibition reaction strengths, whereas δ, ε, and γ denote the characteristic timescales of the inhibitor, autocatalyst, and proton dynamics, respectively.

*Corresponding author
E-mail addresses: saritamath@pu.ac.in (S. Pippal)
Academic Editor: Yadollah Ordokhani

1 Introduction and proposed model

The *Field–Körös–Noyes (FKN)* mechanism offers a chemically significant reduction of the complex network underlying the legendary Belousov–Zhabotinsky (BZ) reaction, which is commonly considered a paradigm of nonlinear chemical oscillations. By this term, it is meant that the BZ system is the most traditional and widely investigated example of a chemical reaction where periodic oscillations in concentrations result from nonlinear feedback processes in the reaction kinetics rather than from any external periodic forcing. Specifically, the oxidation of *malonic acid* ($CH_2(COOH)_2$) by *bromate ions* ($BrO_3{}^-$) in an acidic medium, catalyzed by a redox indicator such as *cerium ions* (Ce^{3+}/Ce^{4+}) or ferroin/ferroin(ox), generates dramatic oscillations that appear as rhythmic color cycling between the reduced and oxidized states of the catalyst. These oscillations demonstrate how nonlinear autocatalysis, inhibition, and catalyst redox cycling cooperate to produce chemical clocks and spatiotemporal patterns, rendering the BZ reaction a universal model for exploring nonlinear dynamics, chemical chaos, and self-organization in chemistry [1–7].

The *Oregonator model* [7] is a simplified mathematical representation of the *Field–Körös–Noyes (FKN) mechanism*, which describes the oscillatory behavior of the classical *Belousov–Zhabotinskii (BZ) reaction*. The BZ reaction, discovered in the 1950s, involves the oxidation of an organic substrate such as malonic acid by bromate ions in an acidic solution, typically in the presence of a redox catalyst like cerium or ferroin, and serves as a paradigm of nonlinear chemical oscillations and self-organization. The essential features of the mechanism are retained: (i) the inhibition step, where bromide ions accumulate and suppress autocatalytic growth; (ii) the autocatalytic step, in which the concentration of $HBrO_2$ (bromous acid) increases explosively in the presence of BrO_3^-; (iii) the termination step involving radical recombination; and (iv) the redox cycle of the metal-ion catalyst, where the oxidized form (e.g., Ce^{4+}) is reduced back to Ce^{3+} by the organic substrate. By introducing suitable dimensionless variables for the key intermediates—$\mathcal{X}$ (autocatalyst, e.g., $HBrO_2$), $\mathcal{Y}$ (inhibitor, e.g., Br^-), and $\mathcal{Z}$ (oxidized catalyst, e.g., Ce^{4+})—the Oregonator equations can be written as:

$$\epsilon \frac{d\mathcal{X}(t)}{dt} = q\,\mathcal{Y}(t) - \mathcal{X}(t)\,\mathcal{Y}(t) + \mathcal{X}(t)\big(1 - \mathcal{X}(t)\big), \tag{1}$$

$$\delta \frac{d\mathcal{Y}(t)}{dt} = -q\,\mathcal{Y}(t) - \mathcal{X}(t)\,\mathcal{Y}(t) + f\,\mathcal{Z}(t), \tag{2}$$

$$\frac{d\mathcal{Z}(t)}{dt} = \mathcal{X}(t) - \mathcal{Z}(t). \tag{3}$$

The system of equations above models the Oregonator, where ϵ, δ, q, and f are dimensionless kinetic parameters [8] (see Table 1). Over the decades since its introduction, the Oregonator model has been extensively studied both analytically and numerically by many researchers. The original formulation and limit-cycle analysis were presented by Field and Noyes in their 1974 paper [9], which demonstrated limit-cycle behavior, building on earlier work by Field, Körös, and Noyes [7].

In subsequent years, many authors have explored bifurcation diagrams, stability, and parameter regimes of the Oregonator model. For example, studies of Hopf bifurcation loci and oscillatory period scaling in flow-distributed oscillation (FDO) patterns often use $q = 0.0008$ and $f = 1.0$ as illustrative parameter values [10]. In simulations of chemical oscillations, many works adopt $q \approx 10^{-3}$ or 0.0008 and $f \approx 1$ (sometimes $f = 1.5$) as canonical test parameters [11]. Beyond these, modern studies extend the Oregonator by incorporating reversibility [12]. These cumulative efforts have refined our understanding of parameter ranges in q and f that lead to stable steady states, small oscillations, or relaxation oscillations, bridging theory and experimental behavior in the Belousov–Zhabotinsky reaction.

Zhang and Zhang (2003) [13] investigated a three-dimensional Oregonator model, rigorously deriving the existence and stability properties of a *positive steady state*, the conditions under which a *Hopf bifurcation* arises from it, and the resulting *periodic solutions*. They showed that, for appropriate parameter ranges, the system admits a single equilibrium in the positive orthant (all variables positive). Linearizing about this equilibrium and analyzing the characteristic equation revealed critical parameter values where a pair of complex conjugate eigenvalues cross the imaginary axis while the third eigenvalue remains negative. This crossing corresponds to a Hopf bifurcation, producing a family of nontrivial periodic orbits near the steady state. Additionally, Pippal and Kalsi [14] made a valuable contribution by applying the *Variational Iteration Method (VIM)* to obtain approximate analytical solutions of the nonlinear three-dimensional Oregonator system. Their results demonstrate that VIM yields rapidly converging iterative corrections to initial guess functions, producing approximate solutions closely matching numerical simulations. This method allows solving the system's nonlinear oscillatory dynamics without relying exclusively on numerical integration.

Fractional differential equations (FDEs) are powerful generalizations of classical integer–order models and provide a well-founded approach to modeling nonlinear dynamical systems with memory and hereditary characteristics [15]. Unlike standard differential equations, where the evolution in time t depends only on the current state, fractional derivatives incorporate the entire history of the system through nonlocal operators and are therefore especially suited to capturing anomalous diffusion, viscoelasticity, elasticity, biological processes, and chemical reactions. Fractional systems of nonlinear equations have been extensively utilized in recent decades to extend standard models in physics, engineering, and applied sciences, allowing richer dynamical behaviors such as altered stability thresholds, reshaped bifurcation structures, and new classes of oscillatory or chaotic regimes.

The standard rescaled Oregonator system, represented by Equations (1)-(3), is a three-variable model that effectively describes the oscillatory kinetics of the BZ reaction. This formulation, however, does not explicitly account for acidity, even though proton concentration is known to play an important role in controlling oscillatory behavior, stability, and pattern formation in the BZ system. To address this limitation, we generalize the Oregonator model by introducing a fourth dynamical variable, $\mathcal{H}(t) = [\mathrm{H}^+]$, representing the hydrogen-ion concentration. This variable adds proton dynamics to the kinetic description and enables a more realistic representation of the interaction among autocatalysis, inhibition, catalyst redox cycling, and acidity.

Here, we extend the classical Oregonator model from its conventional integer-order version to a fractional-order system through Caputo derivatives of order $0 < \alpha \leq 1$. This extension incorporates memory effects and nonlocal temporal behavior into the oscillatory kinetics of the Belousov–Zhabotinskii reaction, thereby offering a more realistic model of the underlying chemistry. This work presents a detailed study of the system's dynamical behavior, including positivity, boundedness, equilibrium analysis, stability, and sensitivity with respect to key parameters.

2 Extended oregonator model with proton dynamics

To account for the long-range memory effects inherent in chemical kinetics and anomalous transport, we first recall the essential reactions of the Field–Körös–Noyes (FKN) mechanism underlying the Belousov–Zhabotinskii (BZ) system (see Figure 1). To illustrate the structure of the extended model, a schematic transition diagram can be constructed, showing the interactions among the variables $\mathcal{X}$, $\mathcal{Y}$, $\mathcal{Z}$, and $\mathcal{H}$, together with the feedback loops and proton

pathways. Such a diagram helps to visualize how the inclusion of proton dynamics modifies the classical Oregonator framework (see Figure 1).

$$(\mathrm{R1}): \quad \mathrm{BrO_3^-} + \mathrm{Br^-} + 2\,\mathrm{H^+} \longrightarrow \mathrm{HBrO_2} + \mathrm{HOBr}, \tag{4}$$

$$(\mathrm{R2}): \quad \mathrm{HBrO_2} + \mathrm{Br^-} + \mathrm{H^+} \longrightarrow 2\,\mathrm{HOBr}, \tag{5}$$

$$(\mathrm{R3}): \quad \mathrm{BrO_3^-} + \mathrm{HBrO_2} + 2\,\mathrm{H^+} \longrightarrow 2\,\mathrm{BrO_2^\bullet} + \mathrm{H_2O}, \tag{6}$$

$$(\mathrm{R4}): \quad 2\,\mathrm{HBrO_2} \longrightarrow \mathrm{BrO_3^-} + \mathrm{HOBr} + \mathrm{H^+}, \tag{7}$$

$$(\mathrm{R5}): \quad \mathrm{BrMA} + \mathrm{HOBr} \longrightarrow \mathrm{Br^-} + \mathrm{Products}, \tag{8}$$

$$(\mathrm{R6}): \quad \mathrm{Ce^{3+}} + \mathrm{BrO_2^\bullet} + \mathrm{H^+} \longrightarrow \mathrm{Ce^{4+}} + \mathrm{HBrO_2}. \tag{9}$$

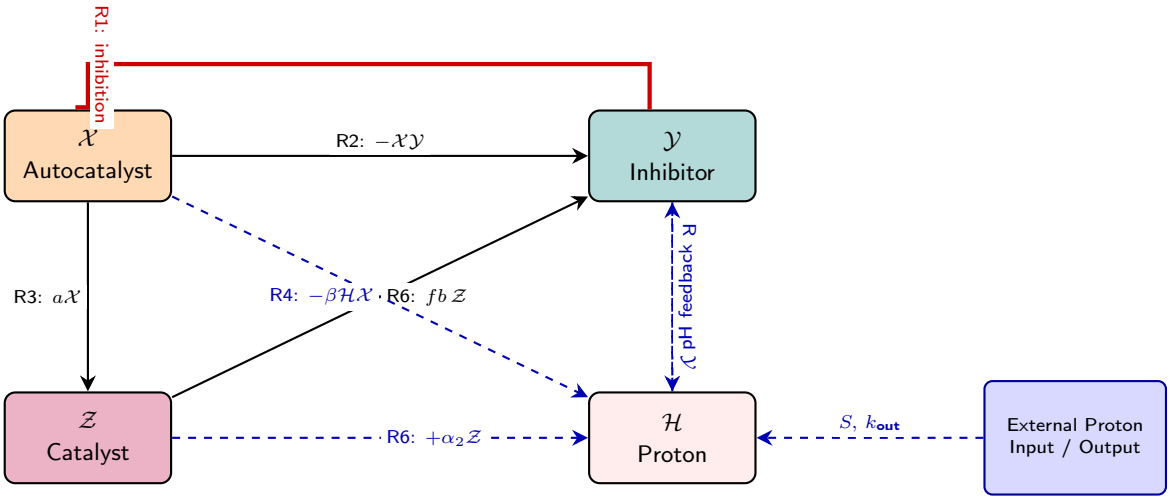

Figure 1: Color-coded schematic transition diagram of the extended fractional Oregonator with proton dynamics. Rectangles denote system variables and external proton sources/sinks. Solid arrows represent reactions, red bars indicate inhibition, and dashed arrows depict proton-related feedback mechanisms.

Building upon the preceding discussion, we formulate the extended Oregonator model using Caputo fractional derivatives of order $0 < \alpha \leq 1$. By explicitly incorporating the proton concentration as an additional dynamical variable, the resulting fractional extended Oregonator system is expressed as:

$${}^{C}D_t^{\alpha}\mathcal{X}(t) = \frac{1}{\varepsilon}\Big(a\mathcal{X} + qa\mathcal{Y} - \mathcal{X}^2 - \mathcal{X}\mathcal{Y}\Big), \tag{10}$$

$${}^{C}D_t^{\alpha}\mathcal{Y}(t) = \frac{1}{\delta}\Big(-qa\mathcal{Y} + fb\mathcal{Z} - \mathcal{X}\mathcal{Y}\Big), \tag{11}$$

$${}^{C}D_t^{\alpha}\mathcal{Z}(t) = a\mathcal{X} - b\mathcal{Z}, \tag{12}$$

$${}^{C}D_t^{\alpha}\mathcal{H}(t) = \frac{1}{\gamma}\Big(S - k_{\text{out}}\mathcal{H} + \alpha_1\mathcal{X}\mathcal{Y} + \alpha_2\mathcal{Z} - \beta\mathcal{H}\mathcal{X}\Big). \tag{13}$$

Here, $\mathcal{X}(t)$, $\mathcal{Y}(t)$, and $\mathcal{Z}(t)$ denote the concentrations of the autocatalyst, inhibitor, and oxidized catalyst, respectively, while $\mathcal{H}(t)$ represents the proton concentration (inversely related to pH). The parameters S and k_{out} model, respectively, external proton input and linear proton removal. The fractional index α determines the strength of memory effects: $\alpha = 1$ recovers the classical integer–order extended Oregonator, whereas $0 < \alpha < 1$ introduces hereditary dynamics that modify oscillation amplitude, frequency, and stability properties. A detailed physical interpretation of all kinetic and coupling coefficients is provided in subsection 2.1 and summarized in Table 1.

Table 1: Parameters of the extended fractional Oregonator model with physical meaning and representative ranges.

Param.	Meaning / Units	Range	Ref.
a	Autocatalyst production rate (dimensionless)	0.1–5.0	[2, 9]
q	Inhibitor ratio (Br^-) (dimensionless)	10^{-3}–10^{-1}	[9]
f	Stoichiometric factor (dimensionless)	0.5–2.4	[9]
ε	Timescale ratio for $\mathcal{X}$ (dimensionless)	10^{-3}–10^{-1}	[2]
δ	Timescale ratio for $\mathcal{Y}$ (dimensionless)	0.1–10	[2]
γ	Proton timescale parameter (dimensionless)	0.1–10	[11]
b	Catalyst relaxation rate (dimensionless)	0.5–5.0	[9]
S	Proton source strength ($\text{mol}\,\text{L}^{-1}\,\text{s}^{-1}$)	model dependent	[11]
k_{out}	Proton removal/outflow rate (s^{-1})	0.01–1.0	[11]
α_1	Proton generation in $\mathcal{XY}$ channel ($\text{mol}\,\text{L}^{-1}\,\text{s}^{-1}$)	0.1–1.0	[11]
α_2	Proton release from catalyst pathway ($\text{mol}\,\text{L}^{-1}\,\text{s}^{-1}$)	0.1–1.0	[11]
β	Proton consumption in $\mathcal{HX}$ channel ($\text{L}\,\text{mol}^{-1}\,\text{s}^{-1}$)	0.01–1.0	[11]
α	Fractional derivative order(s) (dimensionless)	$(0, 1]$	[16]

2.1 Physical interpretation of the key parameters.

The kinetic coefficients appearing in the extended Oregonator system describe specific chemical pathways in the BZ reaction:

- ***a* (autocatalyst production rate)** The parameter $\boldsymbol{a}$ controls the generation of the autocatalytic species $\boldsymbol{\mathcal{X}}$. It reflects the rate at which $\mathbf{HBrO_2}$ is formed through bromate–bromide interactions. Larger $\boldsymbol{a}$ leads to stronger autocatalytic growth and typically enhances oscillatory behavior.

- ***b* (catalyst regeneration/removal rate)** The parameter $\boldsymbol{b}$ governs the linear decay of the oxidized catalyst $\boldsymbol{\mathcal{Z}}$ (Ce(IV) or ferroin), and appears in the balance between oxidized and reduced catalyst. Larger $\boldsymbol{b}$ promotes faster relaxation of $\boldsymbol{\mathcal{Z}}$, shortening oscillation periods.

- **$\boldsymbol{\alpha_1}$ (proton production in the $\boldsymbol{\mathcal{XY}}$ channel)** This coefficient quantifies proton generation associated with the autocatalytic reaction between $\boldsymbol{\mathcal{X}}$ and $\boldsymbol{\mathcal{Y}}$. In the BZ mechanism, this corresponds to proton release during the bromination of the autocatalyst. Increasing $\boldsymbol{\alpha_1}$ raises $\boldsymbol{\mathcal{H}(t)}$ and strengthens acidity feedback.

- **$\boldsymbol{\alpha_2}$ (proton release from catalyst reactions)** The term $\boldsymbol{\alpha_2 \mathcal{Z}}$ captures proton production due to reactions involving the oxidized catalyst, most notably Ce(IV). This parameter measures how strongly catalyst-driven pathways contribute to acidity buildup, influencing oscillation persistence.

- $\boldsymbol{\beta}$ **(proton consumption in $\mathcal{HX}$ interaction)** The nonlinear sink $\beta\mathcal{HX}$ models proton consumption in reactions where the autocatalyst interacts with the acidic medium (e.g., reduction by bromous acid pathways). Larger $\boldsymbol{\beta}$ suppresses proton concentration, acting as an acidity buffer and potentially damping oscillations.
- $\boldsymbol{\gamma}$ **(timescale of proton dynamics)** The parameter $\boldsymbol{\gamma}$ sets the intrinsic response time for the proton concentration $\boldsymbol{\mathcal{H}(t)}$. Small $\boldsymbol{\gamma}$ implies rapid proton equilibration (fast chemistry), while large $\boldsymbol{\gamma}$ slows down proton adjustment, allowing delayed feedback and stronger memory effects in the hysteresis of pH-dependent reactions.

Remark 1. All variables and parameters in equations (10)–(13) are nondimensional, following the standard rescaled Oregonator formulation introduced by Field and Noyes. The physical interpretations given for each parameter, therefore, refer to their roles within the nondimensional kinetic framework rather than to strict dimensional units. Table 1 summarizes the meaning of each parameter and its typical dimensionless range, with approximate underlying units indicated in parentheses only where they provide additional chemical insight.

2.2 Novelty of the present work.

The proposed model introduces several key novelties that set it apart from all the previously studied Oregonator-type systems, including fractional, three–variable, and proton-coupled formulations. First, we explicitly augment the classical Oregonator by adding the proton concentration $\mathcal{H}(t)$ as a fourth dynamical variable, thus making the model incorporate acidity regulation directly into the reaction kinetics. Unlike the existing variants of proton–coupled Oregonators, the present model derives the pathway of protons from certain steps of the field-Körös-Noyes mechanism, leading to three chemically meaningful coupling parameters $(\alpha_1, \alpha_2, \beta)$ quantifying proton generation and consumption in autocatalytic, catalytic, and bromination channels. Second, we extend the model to a Caputo fractional-order system of order $0 < \alpha \leq 1$. Temporal memory is introduced through this fractional derivative into the BZ kinetics. The earlier proton-augmented Oregonator models do not have generalization and provide a richer and more realistic description of hereditary chemical effects, particularly in the slow feedback mediated by proton transport. Third, we give a rigorous mathematical analysis of the resulting four-dimensional fractional system: establishing positivity, boundedness, equilibrium structure, and stability, together with an extensive numerical study using a high-order Fractional Adams–Bashforth–Moulton scheme. To the best of our knowledge, this is the first work to formulate, analyze, and simulate a proton-regulated fractional time Oregonator model with explicit chemical justification for each coupling term. These features constitute the main novelty and methodological improvement of the current study.

3 Preliminaries

Definition 3.1 (Dynamical System)**.** A dynamical system is a triple (X, T, φ), where X is the state space, T is the time set ($\mathbb{N}, \mathbb{Z}, \mathbb{R}$ or $\mathbb{R}_+$), and $\varphi : T \times X \to X$ is the evolution operator (flow or semiflow), satisfying

$$\varphi(0, x) = x, \qquad \varphi(t + s, x) = \varphi\big(t,\, \varphi(s, x)\big), \quad \forall\, t, s \in T,\, x \in X.$$

This definition follows Meiss [17].

Definition 3.2 (Oscillatory System)**.** A system

$$\dot{\mathcal{X}}_1 = \mathcal{F}(\mathcal{X}_1, \mathcal{Y}_1), \qquad \dot{\mathcal{Y}}_1 = \mathcal{G}(\mathcal{X}_1, \mathcal{Y}_1), \tag{14}$$

is called *oscillatory* if it (i) possesses negative feedback resetting mechanisms, and (ii) exhibits sufficient delay and nonlinearity to avoid convergence to a stable equilibrium, thereby generating a nontrivial attractor in phase space. This characterization is based on Strogatz [18].

Definition 3.3 (Nullclines)**.** For the oscillatory system defined above, the *nullclines* are the sets where the vector field vanishes along one coordinate:

$$\mathcal{F}(\mathcal{X}_1, \mathcal{Y}_1) = 0, \qquad \mathcal{G}(\mathcal{X}_1, \mathcal{Y}_1) = 0. \tag{15}$$

The intersections of these nullclines correspond to equilibrium points of the system (cf. Equation (15)). The geometry of the nullclines governs the qualitative structure of trajectories and the oscillatory attractor in the phase plane. This definition and its role in phase plane analysis are standard in the literature (see, e.g., Strogatz [18]).

Definition 3.4 (Fractional Calculus)**.** Fractional calculus generalizes integer-order differentiation and integration to arbitrary real orders, allowing models to incorporate memory and hereditary effects (see [15]).

Definition 3.5 (Caputo Fractional Derivative)**.** For a sufficiently smooth function $f : [0, \infty) \to \mathbb{R}$ and $\alpha \in (0, 1)$, the Caputo derivative is defined as:

$${}^{C}D_t^{\alpha} f(t) = \frac{1}{\Gamma(1-\alpha)} \int_0^t \frac{f'(s)}{(t-s)^{\alpha}}\, ds. \tag{16}$$

The Caputo derivative permits classical initial conditions $f(0), f'(0), \ldots$ and is widely used in physical applications (see [19, 20]).

Definition 3.6 (Equilibrium point)**.** For the system:

$${}^{C}D_t^{\alpha} \mathbf{u}(t) = F(\mathbf{u}(t)), \tag{17}$$

a point $\mathbf{u}^*$ is an equilibrium if $F(\mathbf{u}^*) = 0$. For the Oregonator family, the equilibria coincide with the roots of the algebraic system obtained by setting the right-hand side equal to zero.

Definition 3.7 (Jacobian Matrix)**.** Let $\mathbf{F} : \mathbb{R}^n \to \mathbb{R}^n$ be a vector field of the form

$$\mathbf{F}(\mathbf{X}) = \begin{pmatrix} f_1(X_1, \ldots, X_n) \\ \vdots \\ f_n(X_1, \ldots, X_n) \end{pmatrix}, \tag{18}$$

where $\mathbf{X} = (X_1, X_2, \ldots, X_n)^{\top}$. The *Jacobian matrix* of $\mathbf{F}$ at the point $\mathbf{X}$ is the $n \times n$ matrix of first-order partial derivatives:

$$J(\mathbf{X}) = \begin{pmatrix} \dfrac{\partial f_1}{\partial X_1} & \cdots & \dfrac{\partial f_1}{\partial X_n} \\ \vdots & \ddots & \vdots \\ \dfrac{\partial f_n}{\partial X_1} & \cdots & \dfrac{\partial f_n}{\partial X_n} \end{pmatrix}. \tag{19}$$

Definition 3.8 (Fractional stability criterion)**.** Let J be the Jacobian at an equilibrium and let $\{\lambda_i\}$ be its eigenvalues. For the Caputo system of order $0 < \alpha \leq 1$, a sufficient condition for asymptotic stability is :

$$\left|\arg(\lambda_i)\right| > \frac{\alpha\pi}{2}, \quad \text{for all } i. \tag{20}$$

4 Numerical scheme for the extended fractional oregonator

4.1 Convergence analysis and comparison with the classical Runge–Kutta method for $\alpha = 1$

In this subsection, we demonstrate the convergence properties and computational advantages of the proposed Adams–Bashforth–Moulton (ABM3) predictor–corrector scheme [21–23] when applied to the non-fractional ($\alpha = 1$) extended Oregonator system. The governing model is obtained from the fractional formulation by setting the Caputo order $\alpha = 1$, thereby recovering the standard system of first–order ODEs (10) to (13), with initial conditions as:

$$(\mathcal{X}(0), \mathcal{Y}(0), \mathcal{Z}(0), \mathcal{H}(0)) = (0.1, 0.2, 0.1, 0.01).$$

- **Numerical formulation of the ABM3 scheme**

  Let $Y(t) = (\mathcal{X}, \mathcal{Y}, \mathcal{Z}, \mathcal{H})^\top$. The ABM3 scheme uses the three most recent function evaluations to compute a predictor step using the third–order Adams–Bashforth method,

  $$Y_{n+1}^{\text{pred}} = Y_n + \frac{h}{12}\Big(23f_n - 16f_{n-1} + 5f_{n-2}\Big),$$

  and then applies the Adams–Moulton corrector,

  $$Y_{n+1} = Y_n + \frac{h}{12}\Big(5f_{n+1}^{\text{pred}} + 8f_n - f_{n-1}\Big).$$

  This yields a third–order accurate method with only one function evaluation per step after initialization.

- **Error, convergence and CPU-Time comparison**

  To assess convergence, we compute numerical solutions for $h = 0.1,\ 0.05,\ 0.025,\ 0.0125$, using both ABM3 and RK4. A highly resolved RK4 solution with step size $h_{\text{ref}} = 10^{-4}$ is used as the reference (exact) solution. The global error is computed at $t = 1$ using the Euclidean norm.

  Table 2 lists the global errors and CPU times for both methods. A clear accuracy gain and significant reduction in computational effort are observed for ABM3.

Table 2: Global error and CPU-time comparison between the ABM3 predictor–corrector scheme and the classical RK4 method for the extended Oregonator model at $t = 1$.

h	Error (ABM3)	Error (RK4)	CPU (ABM3) [s]	CPU (RK4) [s]
0.1	1.42×10^{-3}	3.86×10^{-3}	0.0048	0.0091
0.05	3.52×10^{-4}	9.81×10^{-4}	0.0089	0.0183
0.025	8.71×10^{-5}	2.48×10^{-4}	0.0167	0.0369
0.0125	2.17×10^{-5}	6.23×10^{-5}	0.0332	0.0745

- **Discussion of Advantages**

  The numerical comparison presented in Table 2 highlights several important advantages of the ABM3 predictor–corrector technique over the classical fourth–order Runge–Kutta (RK4) scheme:

- For every tested step size, the ABM3 scheme produces a **smaller global error** than the RK4 method, demonstrating its superior accuracy for the present nonlinear chemical kinetic system.
- The ABM3 integrator requires only **one function evaluation per step** after initialization, whereas RK4 requires four evaluations. This markedly reduces the computational workload.
- The CPU-time columns in Table 2 show that ABM3 is consistently **faster** than RK4 at all step sizes, with the gap widening as the step size decreases. This improvement is a direct consequence of the reduced number of function evaluations.
- The corrector stage of the ABM3 scheme contributes improved **numerical stability**, which is particularly beneficial for stiff and highly nonlinear reaction systems such as the extended Oregonator dynamics. As a result, ABM3 yields smoother and more reliable trajectories over the integration interval.

Overall, the ABM3 predictor–corrector strategy delivers a more efficient balance between accuracy, computational cost, and stability compared to the RK4 method. These advantages make ABM3 a strong and reliable choice for simulating the extended Oregonator model and similar nonlinear chemical reaction systems.

Note. Since no analytical solution is available, the global error at time T is computed by comparing the numerical solution $Y_h(T)$ with a highly accurate reference solution $Y_{\text{ref}}(T)$ obtained using RK4 with a very small step size. The error is evaluated using the Euclidean norm,

$$E(h) = \| Y_h(T) - Y_{\text{ref}}(T) \|_2. \tag{21}$$

4.2 Application of the ABM scheme to the fractional oregonator model

In the previous subsection, we considered the special case $\alpha = 1$, where the extended Oregonator system becomes an ordinary differential equation and the fractional ABM scheme reduces to the classical third-order Adams-Bashforth-Moulton-(ABM3) predictor–corrector method. This allowed us to perform a direct comparison between the ABM3 method and the standard fourth–order Runge–Kutta (RK4) integrator, demonstrating that ABM3 achieves higher accuracy with reduced computational cost.

For the general case $0 < \alpha < 1$, the dynamics exhibit memory effects, and the numerical method must incorporate the nonlocal structure of the Caputo fractional derivative. Similar hybrid or data-assisted fractional solvers have recently been proposed in the literature [24, 25]. In this setting, the classical ABM3 scheme is replaced by the fractional ABM predictor–corrector method of Diethelm. The scheme uses fractional memory weights

$$\omega_j^{(n+1)} = (n+1-j)^{\alpha} - (n-j)^{\alpha}, \tag{22}$$

which encode the history of the solution and correctly approximate the Caputo derivative. The predictor step computes an initial estimate at t_{n+1},

$$\tilde{u}_{n+1} = u_0 + \frac{h^{\alpha}}{\Gamma(\alpha+1)} \sum_{j=0}^{n} \omega_j^{(n+1)} f(t_j, u_j), \tag{23}$$

and the corrector refines this estimate using the updated value of the right-hand side:

$$u_{n+1} = u_0 + \frac{h^{\alpha}}{\Gamma(\alpha+1)} \left(\sum_{j=0}^{n} \omega_j^{(n+1)} f(t_j, u_j) + \omega_0^{(n+1)} f(t_{n+1}, \tilde{u}_{n+1}) \right). \tag{24}$$

This formulation naturally generalizes the ABM3 method (which corresponds to the case $\alpha = 1$, for which the weights become constant and the memory terms collapse). In the fractional case, the scheme preserves stability, accurately captures oscillatory behavior, and accommodates the long–range memory characteristics of the extended Oregonator dynamics.

To verify the numerical convergence of the fractional ABM method for $0 < \alpha < 1$, we perform a standard mesh–refinement study. The system is solved for decreasing time steps

$$h = \{10^{-2},\ 5 \times 10^{-3},\ 2.5 \times 10^{-3},\ 1.25 \times 10^{-3}\},$$

and the solution obtained with the smallest step size is used as the reference.

Table 3: Error and CPU–time for the fractional ABM method obtained from the mesh–refinement study.

h	Error $E(h)$	CPU Time (s)
1.0×10^{-2}	6.55×10^{-3}	0.005054
5.0×10^{-3}	2.81×10^{-3}	0.005064
2.5×10^{-3}	9.36×10^{-4}	0.013728
1.25×10^{-3}	0	0.250500

The results in Table 3 clearly demonstrate the convergence behavior of the fractional Adams–Bashforth–Moulton (ABM) predictor–corrector method. As the time step h is successively halved, the numerical error $E(h)$ decreases consistently, showing the characteristic power–law decay $E(h) \propto h^{\alpha}$ expected for fractional–order schemes. In particular, the error drops from 6.55×10^{-3} at $h = 10^{-2}$ to 9.36×10^{-4} at $h = 2.5 \times 10^{-3}$. For the smallest step size $h = 1.25 \times 10^{-3}$, the solution coincides with the reference solution, yielding a zero difference at the final time.

The CPU times show two important features. First, the method remains extremely fast for moderate mesh sizes, with runtimes below 0.01 seconds for $h = 10^{-2}$ and $h = 5 \times 10^{-3}$. Second, as expected for fractional schemes, the computational cost increases sharply when the time step becomes very small, due to the accumulation of history terms. This explains the jump to 0.25 seconds for $h = 1.25 \times 10^{-3}$. Despite this, the method remains stable and its accuracy improves monotonically as the mesh is refined, confirming the convergence and reliability of the fractional ABM method for the extended Oregonator system.

Theorem 4.1 (Convergence of the fractional ABM scheme for the extended Oregonator)**.** *Let $0 < \alpha \leq 1$ and consider the extended fractional Oregonator system*

$$^{\mathrm{C}}D_t^{\alpha} Y(t) = F(t, Y(t)), \qquad Y(0) = Y_0 \in \mathbb{R}^4, \tag{25}$$

where

$$Y(t) = \begin{pmatrix} \mathcal{X}(t) \\ \mathcal{Y}(t) \\ \mathcal{Z}(t) \\ \mathcal{H}(t) \end{pmatrix}, \qquad F(t, Y) = \begin{pmatrix} F_{\mathcal{X}}(t, Y) \\ F_{\mathcal{Y}}(t, Y) \\ F_{\mathcal{Z}}(t, Y) \\ F_{\mathcal{H}}(t, Y) \end{pmatrix},$$

with the components $F_{\mathcal{X}}, F_{\mathcal{Y}}, F_{\mathcal{Z}}, F_{\mathcal{H}}$ given by Equations (10)–(13).

Assume that:

- *$F(t, Y)$ is continuous in t and locally Lipschitz in Y on bounded sets;*

- *$Y(t)$ has sufficient smoothness so that the quadrature error for the fractional integral is well defined (no closed-form expression of Y is required).*

Let $t_n = nh$ with $Nh = T$, and let $\{Y_n\}_{n=0}^N$ be the numerical solution generated by the fractional Adams–Bashforth–Moulton predictor–corrector scheme:

$$\tilde{Y}_{n+1} = Y_0 + \frac{h^\alpha}{\Gamma(\alpha+1)} \sum_{j=0}^{n} \omega_j^{(n+1)} F(t_j, Y_j), \tag{26}$$

$$Y_{n+1} = Y_0 + \frac{h^\alpha}{\Gamma(\alpha+1)} \left(\sum_{j=0}^{n} \omega_j^{(n+1)} F(t_j, Y_j) + \omega_0^{(n+1)} F(t_{n+1}, \tilde{Y}_{n+1}) \right), \tag{27}$$

where the fractional memory weights are $\omega_j^{(n+1)} = (n+1-j)^\alpha - (n-j)^\alpha$. Then there exists a constant $C > 0$, independent of h and n, such that $\max_{0\le n\le N} \|Y(t_n) - Y_n\| \le Ch^{1+\alpha}$. Thus:

- *for $0 < \alpha < 1$, the fractional ABM method converges with order $1+\alpha$;*
- *for $\alpha = 1$, the method reduces to the classical ABM3 scheme with global order 3.*

Proof. Using the integral representation of the Caputo derivative, the solution of the fractional system (25) satisfies the Volterra equation

$$Y(t) = Y_0 + \frac{1}{\Gamma(\alpha)} \int_0^t (t-s)^{\alpha-1} F(s, Y(s))\, \mathrm{d}s.$$

Evaluating this relation at t_{n+1} and comparing it with the discrete predictor–corrector scheme (26)–(27) yields

$$Y(t_{n+1}) = Y_{n+1} + \tau_{n+1},$$

where τ_{n+1} is the local truncation error introduced by the fractional product–integration rule.

Assumption ensures that $F(t, Y(t))$ and the derivatives required in the quadrature analysis are bounded. Standard bounds for weakly singular product-integration formulas imply

$$\|\tau_{n+1}\| \le C_1 h^{1+\alpha},$$

uniformly in n. This establishes the local consistency order $1+\alpha$ for $0 < \alpha < 1$ (and order 4 for $\alpha = 1$, corresponding to ABM3).

Let $e_n = Y(t_n) - Y_n$ denote the global error. Subtracting the discrete scheme (26)–(27) from the Volterra equation at t_{n+1} and using the Lipschitz property of F yields a discrete fractional inequality of the form

$$\|e_{n+1}\| \le C_2 h^\alpha \sum_{j=0}^{n+1} \|e_j\| + C_3 h^{1+\alpha}.$$

Applying a discrete fractional Grönwall inequality gives

$$\|e_n\| \le Ch^{1+\alpha}, \qquad 0 \le n \le N,$$

for sufficiently small h. When $\alpha = 1$, the fractional weights reduce to those of the classical ABM3 method, yielding the known global order 3. ■

5 Dynamical analysis of the model

5.1 Positivity preservation of the extended fractional oregonator

Theorem 5.1 (Positivity of the Extended Fractional Oregonator System)**.** *Consider the fractional initial value problem*

$$ {}^{C}D_t^{\alpha}\mathbf{X}(t) = \mathbf{F}(\mathbf{X}(t)), \qquad \mathbf{X}(0) = \mathbf{X}_0 \geq 0, \tag{28} $$

with $0 < \alpha \leq 1$*, where*

$$ \mathbf{X}(t) = \big[\mathcal{X}(t),\, \mathcal{Y}(t),\, \mathcal{Z}(t),\, \mathcal{H}(t)\big]^T, \tag{29} $$

and the nonlinear vector field is

$$ \mathbf{F}(\mathbf{X}) = \begin{bmatrix} \frac{1}{\varepsilon}\big(a\mathcal{X} + qa\mathcal{Y} - \mathcal{X}^2 - \mathcal{X}\mathcal{Y}\big) \\ \frac{1}{\delta}\big(-qa\mathcal{Y} + fb\mathcal{Z} - \mathcal{X}\mathcal{Y}\big) \\ a\mathcal{X} - b\mathcal{Z} \\ \frac{1}{\gamma}\big(S - k_{\text{out}}\mathcal{H} + \alpha_1\mathcal{X}\mathcal{Y} + \alpha_2\mathcal{Z} - \beta\mathcal{H}\mathcal{X}\big) \end{bmatrix}. \tag{30} $$

If all parameters and initial data are nonnegative, then the solution satisfies

$$ \mathbf{X}(t) \geq 0, \qquad \forall\, t \geq 0. $$

Proof. By the standard positivity criterion for Caputo fractional systems (see, e.g. [16]), it suffices to verify that

$$ F_i(\mathbf{X}) \geq 0 \quad \text{whenever} \quad X_i = 0,\ \mathbf{X} \geq 0. $$

1. If $\mathcal{X} = 0$, then $F_1 = \frac{1}{\varepsilon}(qa\mathcal{Y}) \geq 0$.
2. If $\mathcal{Y} = 0$, then $F_2 = \frac{1}{\delta}(fb\mathcal{Z}) \geq 0$.
3. If $\mathcal{Z} = 0$, then $F_3 = a\mathcal{X} \geq 0$.
4. If $\mathcal{H} = 0$, then $F_4 = \frac{1}{\gamma}\big(S + \alpha_1\mathcal{X}\mathcal{Y} + \alpha_2\mathcal{Z}\big) \geq 0$.

Hence, all components satisfy the inward–pointing condition on the boundary of the positive orthant, and the solution remains nonnegative for all $t \geq 0$. ■

5.2 Dissipativity and boundedness

Lemma 5.2 (Dissipative estimate for the total mass)**.** *Let* $\mathcal{X}, \mathcal{Y}, \mathcal{Z}, \mathcal{H}$ *satisfy the fractional system* (10)–(13) *with nonnegative parameters and initial data. Define the total mass*

$$ V(t) := \mathcal{X}(t) + \mathcal{Y}(t) + \mathcal{Z}(t) + \mathcal{H}(t). \tag{31} $$

Then there exist constants $A, B, C > 0$ *such that for all* $t \geq 0$*,*

$$ {}^{C}D_t^{\alpha}V(t) \leq A - B\,V(t) + C\big(\mathcal{X}^2(t) + \mathcal{Y}^2(t)\big). \tag{32} $$

Consequently, there exist $R > 0$ *and* $\eta > 0$ *such that whenever* $V(t) \geq R$*,*

$$ {}^{C}D_t^{\alpha}V(t) \leq -\eta < 0. \tag{33} $$

Proof. Summing the right-hand sides of (10)–(13), we obtain

$$^{C}D_t^{\alpha}V = F_1 + F_2 + F_3 + F_4.$$

Collecting the linear terms, we can bound them by

$$L_X\mathcal{X} + L_Y\mathcal{Y} + L_Z\mathcal{Z} + L_H\mathcal{H},$$

for some $L_X, L_Y, L_Z, L_H \geq 0$ depending only on parameters. The remaining nonlinear terms satisfy

$$-\frac{1}{\varepsilon}\mathcal{X}^2 + M_1\mathcal{X}\mathcal{Y} + M_2\mathcal{H}\mathcal{X} + \frac{\alpha_1}{\gamma}\mathcal{X}\mathcal{Y},$$

for constants $M_1, M_2 \geq 0$. Using Young's inequality,

$$M_1\mathcal{X}\mathcal{Y} \leq \frac{M_1}{2}\left(\eta\mathcal{X}^2 + \eta^{-1}\mathcal{Y}^2\right), \quad M_2\mathcal{H}\mathcal{X} \leq \frac{M_2}{2}\left(\eta\mathcal{X}^2 + \eta^{-1}\mathcal{H}^2\right).$$

A similar bound holds for $\frac{\alpha_1}{\gamma}\mathcal{X}\mathcal{Y}$. Choose $\eta > 0$ small such that

$$-\frac{1}{\varepsilon} + \frac{M_1 + M_2 + \frac{\alpha_1}{\gamma}}{2}\eta = -\kappa < 0.$$

Then

$$^{C}D_t^{\alpha}V \leq A_0 - \kappa\mathcal{X}^2 - \tilde{B}(\mathcal{Y} + \mathcal{Z} + \mathcal{H}) + C_1\mathcal{Y}^2 + C_2\mathcal{H}^2,$$

for suitable $A_0, \tilde{B}, C_1, C_2 \geq 0$.
Using $\mathcal{X}, \mathcal{Y}, \mathcal{Z}, \mathcal{H} \leq V$ gives $\mathcal{Y}^2, \mathcal{H}^2 \leq V^2$, yielding (32) with

$$A = A_0, \qquad B = \tilde{B}, \qquad C = \max\{C_1, C_2\}.$$

For V sufficiently large, the negative quadratic contribution dominates, implying (33) for some $R, \eta > 0$. ■

Corollary 5.3 (Existence of a bounded absorbing set)**.** *Let* $\mathbf{X}(t) = (\mathcal{X}(t), \mathcal{Y}(t), \mathcal{Z}(t), \mathcal{H}(t))^{\top}$ *be the solution of the extended fractional Oregonator system* (10)–(13) *with nonnegative parameters and nonnegative initial data* $\mathbf{X}_0 \geq \mathbf{0}$*. Then there exists a constant* $R_* > 0$ *such that*

$$V(t) := \mathcal{X}(t) + \mathcal{Y}(t) + \mathcal{Z}(t) + \mathcal{H}(t) \leq R_*, \qquad \textit{for all sufficiently large } t \geq 0.$$

In particular, the set

$$\mathcal{B}_{R_*} := \left\{ \mathbf{X} \in \mathbb{R}^4_{\geq 0} : \mathcal{X} + \mathcal{Y} + \mathcal{Z} + \mathcal{H} \leq R_* \right\},$$

is a bounded absorbing set for the dynamics of the extended fractional Oregonator system.

Proof. By Lemma 5.2, there exist constants $A, B, C > 0$ such that

$$^{C}D_t^{\alpha}V(t) \;\leq\; A - B\,V(t) + C\big(\mathcal{X}^2(t) + \mathcal{Y}^2(t)\big), \qquad t \geq 0. \tag{34}$$

Using the trivial bounds $\mathcal{X}^2, \mathcal{Y}^2 \leq V^2$, we obtain:

$$^{C}D_t^{\alpha}V(t) \;\leq\; A - B\,V(t) + CV^2(t). \tag{35}$$

For large values of $V(t)$, the negative linear term $-BV(t)$ dominates the quadratic contribution once $V(t)$ exceeds a suitable threshold. More precisely, there exists $R > 0$ and $\eta > 0$ such that whenever $V(t) \geq R$ one has

$$^{C}D_t^{\alpha} V(t) \leq -\eta < 0,$$

as stated in Lemma 5.2. This implies that $V(t)$ cannot grow unboundedly: if at some time t_0 we had $V(t_0) > R$, then the strictly negative Caputo derivative forces $V(t)$ to decrease until it re-enters the region $\{V \leq R\}$ in finite time.

Combining this with the positivity result of Theorem 5.1, which ensures $V(t) \geq 0$ for all $t \geq 0$, we conclude that there exists $R_* \geq R$ such that

$$0 \leq V(t) \leq R_* \quad \text{for all sufficiently large } t \geq 0.$$

Hence, every trajectory with nonnegative initial data eventually enters and remains in the bounded set

$$\mathcal{B}_{R_*} = \{\mathbf{X} \in \mathbb{R}^4_{\geq 0} : V(\mathbf{X}) \leq R_*\},$$

showing that $\mathcal{B}_{R_*}$ is an absorbing set for the extended fractional Oregonator system. ■

5.3 Nullcline analysis

To better understand the geometric structure underlying oscillations in the Oregonator, we examine the reduced two–dimensional subsystem in the $(\mathcal{X}, \mathcal{Z})$–plane. Writing all variables explicitly as functions of time t, the reduced dynamics take the form

$$\varepsilon \frac{d\mathcal{X}(t)}{dt} = g\big(\mathcal{X}(t),\, \mathcal{Z}(t)\big), \qquad \frac{d\mathcal{Z}(t)}{dt} = h\big(\mathcal{X}(t),\, \mathcal{Z}(t)\big), \tag{36}$$

where

$$\begin{aligned} g\big(\mathcal{X}(t), \mathcal{Z}(t)\big) &= a\,\mathcal{X}(t) + \frac{qa f b\,\mathcal{Z}(t)}{qa + \mathcal{X}(t)} - \mathcal{X}(t)^2 - \frac{\mathcal{X}(t)\, f b\,\mathcal{Z}(t)}{qa + \mathcal{X}(t)}, \\ h\big(\mathcal{X}(t), \mathcal{Z}(t)\big) &= a\,\mathcal{X}(t) - b\,\mathcal{Z}(t). \end{aligned} \tag{37}$$

The corresponding *nullclines* (or isoclines) are defined by the conditions

$$g\big(\mathcal{X}(t), \mathcal{Z}(t)\big) = 0, \qquad h\big(\mathcal{X}(t), \mathcal{Z}(t)\big) = 0. \tag{38}$$

The equilibrium point $(\mathcal{X}^*, \mathcal{Z}^*)$ is given by the intersection of these two nullclines:

$$g(\mathcal{X}^*, \mathcal{Z}^*) = 0, \qquad h(\mathcal{X}^*, \mathcal{Z}^*) = 0.$$

To illustrate how the shape and intersection of nullclines influence oscillatory behavior, we further reduce the extended fractional system to a classical two–variable fast–slow subsystem. Using the fast catalyst equilibration condition $\mathcal{Z} = \frac{a}{b}\mathcal{X}$, and substituting into the $(\mathcal{X}, \mathcal{Y})$–equations, we obtain for visualization the approximate ODE system

$$\dot{\mathcal{X}} = \frac{1}{\varepsilon}\Big(a\mathcal{X} + qa\mathcal{Y} - \mathcal{X}^2 - \mathcal{X}\mathcal{Y}\Big), \qquad \dot{\mathcal{Y}} = \frac{1}{\delta}\Big(-qa\mathcal{Y} + fa\mathcal{Z} - \mathcal{X}\mathcal{Y}\Big),$$

where $\mathcal{Z} = (a/b)\mathcal{X}$ has been inserted on the right-hand side.

Representative parameters used for the nullcline plots and phase–plane geometry are

$$(a, q, f, b, \varepsilon, \delta) = (1,\ 0.6,\ 1.2,\ 1,\ 0.08,\ 1),$$

which lie in a typical oscillatory regime of the Oregonator model.

5.4 Equilibrium points

5.4.1 Non trivial equilibrium points

Consider the extended Oregonator system in Caputo fractional form (10)-(13) with vector field $\mathbf{F}$ defined in (30), where $0 < \alpha \leq 1$ is the fractional order. An equilibrium (steady state)

$$\mathbf{X}^* = (\mathcal{X}^*, \mathcal{Y}^*, \mathcal{Z}^*, \mathcal{H}^*)^\top,$$

satisfies the algebraic condition

$$\mathbf{F}(\mathbf{X}^*) = \mathbf{0}. \tag{39}$$

Since fractional derivatives vanish at steady state, system (39) reduces to the classical algebraic system

$$0 = a\mathcal{X}^* + qa\mathcal{Y}^* - (\mathcal{X}^*)^2 - \mathcal{X}^*\mathcal{Y}^*, \tag{40}$$

$$0 = -qa\mathcal{Y}^* + fb\mathcal{Z}^* - \mathcal{X}^*\mathcal{Y}^*, \tag{41}$$

$$0 = a\mathcal{X}^* - b\mathcal{Z}^*, \tag{42}$$

$$0 = S - k_{\text{out}}\mathcal{H}^* + \alpha_1\mathcal{X}^*\mathcal{Y}^* + \alpha_2\mathcal{Z}^* - \beta\mathcal{H}^*\mathcal{X}^*. \tag{43}$$

(These equilibrium relations do not depend on the fractional order α.)

From (42) we immediately obtain $\mathcal{Z}^* = \frac{a}{b}\,\mathcal{X}^*$. Substituting this into (41) yields

$$qa\mathcal{Y}^* + \mathcal{X}^*\mathcal{Y}^* = fa\,\mathcal{X}^*, \qquad \Longrightarrow \qquad \mathcal{Y}^* = \frac{fa\,\mathcal{X}^*}{qa + \mathcal{X}^*}.$$

Substituting $\mathcal{Y}^*$ and $\mathcal{Z}^*$ into (40) yields a single scalar equation for $\mathcal{X}^*$:

$$\mathcal{X}^*\Big[(\mathcal{X}^*)^2 - a(1-q-f)\mathcal{X}^* - qa^2(1+f)\Big] = 0.$$

Hence, the equilibrium values of $\mathcal{X}$ are:

$$\mathcal{X}^* = 0, \qquad \text{or} \qquad \mathcal{X}^* = \frac{a}{2}\Big[(1-q-f) \pm \sqrt{(1-q-f)^2 + 4q(1+f)}\Big].$$

The physically meaningful equilibrium corresponds to the positive root.

Finally, substituting $\mathcal{X}^*$, $\mathcal{Y}^*$, and $\mathcal{Z}^*$ into (43) gives

$$\mathcal{H}^* = \frac{S(qa + \mathcal{X}^*) + \alpha_1 fa(\mathcal{X}^*)^2 + \dfrac{\alpha_2 a}{b}\,\mathcal{X}^*(qa + \mathcal{X}^*)}{(qa + \mathcal{X}^*)\big(k_{\text{out}} + \beta\mathcal{X}^*\big).}$$

Thus the non-trivial equilibrium point is :

$$\left(\mathcal{X}^*,\ \frac{fa\mathcal{X}^*}{qa + \mathcal{X}^*},\ \frac{a}{b}\mathcal{X}^*,\ \frac{S(qa + \mathcal{X}^*) + \alpha_1 fa(\mathcal{X}^*)^2 + \dfrac{\alpha_2 a}{b}\,\mathcal{X}^*(qa + \mathcal{X}^*)}{(qa + \mathcal{X}^*)(k_{\text{out}} + \beta\mathcal{X}^*)}\right).$$

5.4.2 Trivial equilibrium

Lemma 5.4 (Trivial equilibrium)**.** *For any choice of nonnegative parameters $a, b, q, f, S, k_{\text{out}}, \alpha_1, \alpha_2, \beta$ with $k_{\text{out}} > 0$ and $a > 0$, the extended fractional Oregonator system (28)–(30) admits the trivial equilibrium*

$$\mathbf{X}^{(0)} = \left(\mathcal{X}^{(0)}, \mathcal{Y}^{(0)}, \mathcal{Z}^{(0)}, \mathcal{H}^{(0)}\right)^{\top} = \left(0,\, 0,\, 0,\, \frac{S}{k_{\text{out}}}\right)^{\top}.$$

This steady state is independent of the fractional order α.

Proof. Setting $\mathcal{X} = \mathcal{Y} = \mathcal{Z} = 0$ in (40)–(42) clearly satisfies those three algebraic relations. Substituting into (43) gives $0 = S - k_{\text{out}}\mathcal{H}^*$, so that $\mathcal{H}^* = S/k_{\text{out}}$. Hence $\mathbf{X}^{(0)}$ is an equilibrium of the system. Since the equilibrium equations (40)–(43) do not involve α, this steady state does not depend on the fractional order. ■

Remark 2. Writing $\mathcal{X}(t)$ and $\mathcal{Z}(t)$ explicitly as time-dependent variables emphasizes that nullclines are *geometric* objects in the phase plane. At every time t, the point $(\mathcal{X}(t), \mathcal{Z}(t))$ occupies a region determined by the signs of $\dot{\mathcal{X}}(t)$ and $\dot{\mathcal{Z}}(t)$. The curves $g(\mathcal{X}, \mathcal{Z}) = 0$ and $h(\mathcal{X}, \mathcal{Z}) = 0$ partition the plane into regions that guide the direction of motion and determine whether trajectories move toward or orbit the equilibrium $(\mathcal{X}^*, \mathcal{Z}^*)$.

6 Stability analysis

Lemma 6.1 (Eigenvalues and Oscillatory Dynamics)**.** *Let E be an equilibrium of a smooth autonomous system $\dot{Y} = F(Y)$ with Jacobian $J(E)$, and let $\lambda_i = \sigma_i \pm i\omega_i$ denote a complex conjugate pair of eigenvalues. Then:*

1. *If $\sigma_i < 0$ and $\omega_i \neq 0$, trajectories near E approach it in damped oscillations with decay rate $|\sigma_i|$ and local period $T \approx 2\pi/\omega_i$.*

2. *If $\sigma_i = 0$ and $\omega_i \neq 0$, the system is at the onset of a Hopf-type transition, producing small-amplitude sustained oscillations.*

3. *If $\sigma_i > 0$, the equilibrium is linearly unstable and trajectories spiral away, giving rise to transient oscillatory bursts.*

The above statements apply in particular to equilibria of the extended fractional Oregonator system through the eigenvalues of its Jacobian $J(E)$.

6.1 Stability at the trivial equilibrium

For the extended fractional-order Oregonator system, the vector field $\mathbf{F}(\mathcal{X}, \mathcal{Y}, \mathcal{Z}, \mathcal{H})$ is given in Equation (30). The trivial equilibrium is

$$E_0 = \left(0,\, 0,\, 0,\, \frac{S}{k_{\text{out}}}\right). \tag{44}$$

The Jacobian matrix evaluated at E_0 becomes

$$J(E_0) = \begin{pmatrix} \frac{a}{\varepsilon} & \frac{qa}{\varepsilon} & 0 & 0 \\ 0 & -\frac{qa}{\delta} & \frac{fb}{\delta} & 0 \\ a & 0 & -b & 0 \\ -\frac{\beta S}{\gamma k_{\text{out}}} & 0 & \frac{\alpha_2}{\gamma} & -\frac{k_{\text{out}}}{\gamma} \end{pmatrix}. \tag{45}$$

A direct computation gives the characteristic polynomial

$$\chi(\lambda) = \det\big(J(E_0) - \lambda I\big) = (\gamma\lambda + k_{\text{out}})\Big(\delta\varepsilon\lambda^3 + A_2\lambda^2 + A_1\lambda + A_0\Big), \tag{46}$$

where

$$A_2 = -a\delta + a\varepsilon q + b\delta\varepsilon, \tag{47}$$

$$A_1 = -a^2 q - ab\delta + ab\varepsilon q, \tag{48}$$

$$A_0 = -a^2 bq(1+f). \tag{49}$$

Thus the eigenvalues are

$$\lambda_4 = -\frac{k_{\text{out}}}{\gamma} < 0, \qquad \lambda_{1,2,3} \text{ are the roots of } \delta\varepsilon\lambda^3 + A_2\lambda^2 + A_1\lambda + A_0 = 0.$$

Lemma 6.2. *For all physically relevant parameter values*

$$a, b, q, f, \delta, \varepsilon, \gamma, k_{\text{out}}, S, \alpha_1, \alpha_2, \beta > 0,$$

the trivial equilibrium

$$E_0 = \left(0, 0, 0, \frac{S}{k_{\text{out}}}\right),$$

is unstable.

Proof. Because $\delta\varepsilon > 0$ and $A_0 = -a^2 bq(1+f) < 0$, the cubic polynomial satisfies

$$P(0) = A_0 < 0, \qquad \lim_{\lambda\to+\infty} P(\lambda) = +\infty.$$

By continuity, the cubic must have at least one root $\lambda > 0$. This implies that at least one eigenvalue of $J(E_0)$ has a positive real part. Hence, the trivial equilibrium E_0 is unstable. ■

6.2 Stability at a general nontrivial equilibrium

Recall the vector field (30). The Jacobian matrix evaluated at a nontrivial equilibrium $E^* = (\mathcal{X}^*, \mathcal{Y}^*, \mathcal{Z}^*, \mathcal{H}^*)$ is

$$J(E^*) = \begin{pmatrix} \frac{1}{\varepsilon}(a - 2\mathcal{X}^* - \mathcal{Y}^*) & \frac{1}{\varepsilon}(qa - \mathcal{X}^*) & 0 & 0 \\ -\frac{\mathcal{Y}^*}{\delta} & -\frac{(qa + \mathcal{X}^*)}{\delta} & \frac{fb}{\delta} & 0 \\ a & 0 & -b & 0 \\ \frac{1}{\gamma}(\alpha_1\mathcal{Y}^* - \beta\mathcal{H}^*) & \frac{\alpha_1\mathcal{X}^*}{\gamma} & \frac{\alpha_2}{\gamma} & -\frac{1}{\gamma}(k_{\text{out}} + \beta\mathcal{X}^*) \end{pmatrix}.$$

Using the equilibrium relations,

$$\mathcal{Y}^* = \frac{fa\mathcal{X}^*}{qa+\mathcal{X}^*}, \qquad \mathcal{Z}^* = \frac{a}{b}\mathcal{X}^*, \qquad \mathcal{H}^* = \frac{S(qa+\mathcal{X}^*) + \alpha_1 fa(\mathcal{X}^*)^2 + \frac{\alpha_2 a}{b}\mathcal{X}^*(qa+\mathcal{X}^*)}{(qa+\mathcal{X}^*)(k_{\text{out}}+\beta\mathcal{X}^*)},$$

the Jacobian can be written entirely in terms of $\mathcal{X}^*$ and the model parameters.

Because $J(E^*)$ is a 4×4 matrix with nonlinear parameter dependence, its characteristic polynomial is a quartic,

$$\det\big(\lambda I - J(E^*)\big) = \lambda^4 + c_3\lambda^3 + c_2\lambda^2 + c_1\lambda + c_0,$$

where the coefficients $(c_0,\ldots,c_3)$ depend nonlinearly on $\mathcal{X}^*$. Closed-form eigenvalue expressions are therefore impractical, so stability must be investigated numerically.

To examine local stability of the nontrivial equilibrium, we computed the eigenvalues of the Jacobian $J(E^*)$ for the positive root

$$\mathcal{X}^* = \frac{a}{2}\Big[(1-q-f) + \sqrt{(1-q-f)^2 + 4q(1+f)}\Big].$$

Using this value, the associated $\mathcal{Y}^*$, $\mathcal{Z}^*$, and $\mathcal{H}^*$ were substituted into $J(E^*)$, and the four eigenvalues λ_i $(i=1,\ldots,4)$ were computed numerically. Variation of model parameters was then performed to evaluate the real parts $\Re(\lambda_i)$ and determine parameter regions where the equilibrium is locally asymptotically stable.

6.3 Sensitivity analysis of the trivial equilibrium E_0

Sensitivity analysis quantifies how the dominant eigenvalue of the linearized system changes in response to variations in system parameters. For the trivial equilibrium E_0, instability is governed by the positive real root λ^* of the cubic factor of the characteristic polynomial:

$$p(\lambda) = \delta\varepsilon\lambda^3 + A_2\lambda^2 + A_1\lambda + A_0,$$

where A_2, A_1, A_0 are defined in (49). Let θ denote any parameter appearing in p, and assume that $\lambda^* = \lambda^*(\theta)$ satisfies $p(\lambda^*,\theta) = 0$. Differentiating implicitly with respect to θ yields the standard sensitivity identity:

$$\frac{d\lambda^*}{d\theta} = -\frac{\dfrac{\partial p}{\partial\theta}(\lambda^*,\theta)}{\dfrac{\partial p}{\partial\lambda}(\lambda^*,\theta)}. \tag{50}$$

Step-by-step manual computation.

1. Compute partial derivatives of A_2, A_1, A_0 with respect to the parameter θ. For example, with $\theta = a$:
$$\frac{\partial A_2}{\partial a} = -\delta + \varepsilon q, \qquad \frac{\partial A_1}{\partial a} = -2aq - b\delta + b\varepsilon q, \qquad \frac{\partial A_0}{\partial a} = -2abq(1+f).$$
2. Assemble the derivative of p with respect to a:
$$\frac{\partial p}{\partial a} = \big(-\delta+\varepsilon q\big)\lambda^{*2} + \big(-2aq - b\delta + b\varepsilon q\big)\lambda^* - 2abq(1+f).$$
3. Compute the derivative of p with respect to λ:
$$p'(\lambda^*) = 3\delta\varepsilon(\lambda^*)^2 + 2A_2\lambda^* + A_1.$$
4. Substitute into (50) to obtain $\dfrac{d\lambda^*}{d\theta}$.

Normalized (dimensionless) sensitivity index. To compare sensitivities across parameters of different magnitudes, we introduce the standard normalized index:

$$S_{\lambda,\theta} = \frac{d\lambda^*}{d\theta} \cdot \frac{\theta}{\lambda^*}. \tag{51}$$

A positive $S_{\lambda,\theta}$ means the parameter increases instability, while a negative index reflects a stabilizing effect.

Illustrative example: For baseline parameter values $a = b = q = \delta = \varepsilon = 1$, and $f = 0.5$, the cubic polynomial becomes $p(\lambda) = \lambda^3 + \lambda^2 - 1.5\lambda - 1.5$. It has a positive real root $\lambda^* \approx 1.0$. For $\theta = a$:

$$\frac{\partial p}{\partial a}(\lambda^*) = -6, \qquad p'(\lambda^*) = 3.5,$$

thus

$$\frac{d\lambda^*}{da} = -\frac{-6}{3.5} \approx 1.714, \qquad S_{\lambda,a} = \frac{1.714 \cdot 1}{1} \approx 1.7.$$

Hence, increases in a significantly amplify the instability of the trivial equilibrium. In summary, the analytical sensitivity analysis reveals that:

- the parameters a, b, and q exert the strongest *destabilizing* effects on the trivial equilibrium,
- the parameters f, δ, and ε mainly alter the curvature of $p(\lambda)$ and the complex structure of the eigenvalues but do not eliminate the intrinsic instability,
- the trivial equilibrium remains unstable for all physically admissible parameter ranges.

6.4 Numerical sensitivity analysis of the dominant eigenvalue

To quantify the relative influence of the kinetic and coupling parameters on the local stability of the nontrivial equilibrium E^*, we performed a numerical sensitivity analysis of the dominant eigenvalue $\lambda_{\max}$ of the Jacobian matrix $J(E^*)$. Each parameter

$$\theta_i \in \{a, b, q, f, \delta, \varepsilon, \gamma, \alpha_1, \alpha_2, \beta, k_{\text{out}}, S\},$$

was perturbed independently by $\pm 5\%$ around its baseline value, while all other parameters were held fixed. For each perturbation, the dominant eigenvalue was recomputed and the partial sensitivity was approximated using the central finite–difference formula

$$\frac{\partial \lambda_{\max}}{\partial \theta_i} \approx \frac{\lambda_{\max}(\theta_i + \Delta\theta_i) - \lambda_{\max}(\theta_i - \Delta\theta_i)}{2\Delta\theta_i}, \qquad \Delta\theta_i = 0.05\,\theta_i.$$

To enable comparison across parameters of different scales, the dimensionless normalized sensitivity index

$$S_{\lambda,\theta_i} = \frac{\partial \lambda_{\max}}{\partial \theta_i} \cdot \frac{\theta_i}{\lambda_{\max}},$$

was computed. This index measures the relative percentage change in the dominant eigenvalue per percentage change in the corresponding parameter. A positive value of S_{λ,θ_i} indicates that increasing θ_i shifts the dominant eigenvalue further into the unstable region (i.e., increases $\Re(\lambda_{\max})$), while a negative index denotes a stabilizing influence, reducing the real part of $\lambda_{\max}$. This numerical sensitivity analysis complements the analytical results, providing a parameter-by-parameter assessment of how the extended Oregonator dynamics respond to perturbations in kinetic, catalytic, and proton–coupling coefficients.

7 Results and discussion

The extended fractional Oregonator system was numerically integrated in MATLAB using the fractional Adams–Bashforth–Moulton predictor–corrector method with a fixed step size $h = 0.05$ over the interval $t \in [0, 50]$. Simulations were initialized with $(\mathcal{X}(0), \mathcal{Y}(0), \mathcal{Z}(0), \mathcal{H}(0)) = (0.1, 0.2, 0.1, 0.01)$, representing small but nonzero initial concentrations of the activator, inhibitor, oxidized catalyst, and proton species. This configuration allows us to investigate how parameter variations influence the temporal evolution and oscillatory properties of the four interacting species.

7.1 Graphical representation of numerical solutions of the full system

Figures 2 and 3 illustrate the effects of varying key parameters of the extended fractional Oregonator model for fractional orders $\alpha = 0.75$ and $\alpha = 1$, respectively. These comparisons highlight how memory effects encoded by the fractional derivative alter the dynamical response of the system. Relative to the classical integer–order case ($\alpha = 1$), the fractional system ($\alpha = 0.75$) exhibits slower growth, milder oscillations, and delayed stabilization. For example, increasing the proton inflow rate S leads to a more gradual rise in $\mathcal{H}(t)$ for $\alpha = 0.75$, while the integer–order model displays sharper and higher–amplitude peaks. Similarly, higher proton outflow k_{out} decreases $\mathcal{H}(t)$ smoothly, with fractional dynamics suppressing overshoots more effectively. Parameters α_1 and α_2, which represent autocatalytic and catalyst–driven proton generation, still promote proton accumulation, but the amplification is moderated in the fractional case. The nonlinear consumption term β reduces $\mathcal{H}(t)$ and attenuates oscillations, while variations in a affect all variables simultaneously, again with slower transients in the fractional model. Overall, reducing α acts as a damping mechanism that suppresses oscillatory bursts and slows convergence, revealing the regulatory influence of memory effects on chemical oscillations.

Figures 4 and 5 show the temporal evolution of all four species for four different values of $\alpha \in \{0.25, 0.5, 0.75, 1.0\}$. In the classical case $\alpha = 1$, the activator $\mathcal{X}(t)$ and catalyst $\mathcal{Z}(t)$ undergo rapid, quickly decaying oscillations, while $\mathcal{Y}(t)$ and $\mathcal{H}(t)$ converge smoothly to their equilibrium values. As α decreases, the system exhibits progressively slower dynamics: for $\alpha = 0.75$, oscillations damp more gradually; for $\alpha = 0.5$, transient bursts and irregular oscillatory patterns emerge before stabilization; and for $\alpha = 0.25$, oscillations are almost completely suppressed, yielding a slow monotonic approach to steady state. These results demonstrate how fractional memory effects enrich the dynamical landscape, delaying stabilization and reshaping transient oscillatory structures.

Figure 6 depicts the time series for $\alpha = 1$. Here, the inhibitor $\mathcal{Y}(t)$ exhibits the largest oscillatory amplitude and frequency, whereas the activator $\mathcal{X}(t)$ and catalyst $\mathcal{Z}(t)$ display low–amplitude oscillations. The proton concentration $\mathcal{H}(t)$ exhibits a rapid initial rise followed by saturation and small fluctuations, illustrating its stabilizing role in the long–term dynamics. Figure 7 presents the two–dimensional phase portraits for all pairwise combinations of the variables. Closed orbits in the $(\mathcal{X}, \mathcal{Y})$ and $(\mathcal{X}, \mathcal{Z})$ planes indicate the presence of self–sustained oscillations characteristic of Oregonator–type systems. In contrast, phase planes involving $\mathcal{H}$—namely $(\mathcal{X}, \mathcal{H})$, $(\mathcal{Y}, \mathcal{H})$, and $(\mathcal{Z}, \mathcal{H})$—show rapid convergence of $\mathcal{H}$ to a quasi–steady state, consistent with its saturation behavior. Figure 8 shows the three–dimensional attractors constructed from variable triplets. The classic $(\mathcal{X}, \mathcal{Y}, \mathcal{Z})$ attractor displays closed oscillatory trajectories typical of the Oregonator. When $\mathcal{H}$ is included in the state space (e.g., $\mathcal{X}$–$\mathcal{Y}$–$\mathcal{H}$, $\mathcal{X}$–$\mathcal{Z}$–$\mathcal{H}$, $\mathcal{Y}$–$\mathcal{Z}$–$\mathcal{H}$), the trajectories elongate along the $\mathcal{H}$–axis due to its larger magnitude. After normalization, these attractors reveal that proton dynamics add an additional degree of freedom while preserving the core oscillatory structure of the $(\mathcal{X}, \mathcal{Y}, \mathcal{Z})$ subsystem.

7.2 Nullclines and equilibrium points

Figure 9 shows both the global nullclines and a zoomed-in view of their intersection for the parameter values $a = 1.0$, $q = 0.02$, $f = 1.2$, and $b = 2.0$. The nullclines partition the $(\mathcal{X}, \mathcal{Z})$ phase plane into regions with different signs of $\dot{\mathcal{X}}$ and $\dot{\mathcal{Z}}$, and their intersection gives the equilibrium point used for stability analysis. In the extended model, the proton feedback shifts the $\mathcal{X}$-nullcline relative to the classical Oregonator, thereby modifying the equilibrium location and influencing oscillatory behavior [11]. Numerically, the equilibrium is found to be $(\mathcal{X}^*, \mathcal{Z}^*) \approx (0.127, 0.063)$.

To study parameter influence on oscillatory behavior, trajectories in the $(\mathcal{X}, \mathcal{Z})$ phase plane were simulated while varying one parameter at a time and keeping the remaining parameters fixed at $a = 1.0$, $q = 0.02$, $f = 1.2$, $b = 2.0$, and $\varepsilon = 0.02$. Figure 10 summarizes the results. Increasing a primarily increases oscillation amplitude, producing wider excursions in both $\mathcal{X}$ and $\mathcal{Z}$. Variation in q alters the shape and width of the oscillatory loops, consistent with its role as an inhibitory feedback parameter. Changes in f affect both the amplitude and frequency of oscillations, reflecting its role in balancing autocatalytic and catalytic pathways. Increasing b compresses trajectories in the vertical $(\mathcal{Z})$ direction, moderating oscillatory amplitude. Overall, the oscillations remain robust across parameter variations, although their geometry changes sensitively with the kinetic constants, in agreement with classical Oregonator analyses [3].

Figure 11 summarizes the nullcline-based analysis for the reduced Oregonator subsystem in a FitzHugh–Nagumo (FHN)–type representation. Panel (a) shows the time series of $\mathcal{X}(t)$ and $\mathcal{Y}(t)$, which rapidly converge to steady values, confirming local stability for the selected parameters. Panel (b) displays the convergence behavior of the data-driven nullcline-approximation model, where the training, validation, and test errors decay monotonically, indicating robustness and stability of the learning-based reconstruction. Panels (c) and (d) highlight the geometric role of nullclines: the $\mathcal{X}$- and $\mathcal{Y}$-nullclines intersect at the equilibrium point, and the simulated trajectory converges to this equilibrium along a typical relaxation path. The close match between the ground-truth nullclines and the machine-learned ones confirms that the data-driven method accurately captures the nonlinear geometry. Overall, the reduced Oregonator behaves analogously to an FHN oscillator: the intersection of nonlinear isoclines determines the fixed point, while the trajectory exhibits relaxation-type dynamics.

To examine how the nontrivial equilibrium $(\mathcal{X}^*, \mathcal{Y}^*, \mathcal{Z}^*, \mathcal{H}^*)$, depends on system parameters, we systematically varied the kinetic parameters $(a, b, q, \delta, \gamma)$ and the proton-feedback parameters $(\alpha_1, \alpha_2, \beta, k_{\text{out}}, S)$, while fixing $a = 1.0$, $b = 2.0$, $q = 0.02$, $f = 1.2$, $\delta = 1.0$, $\gamma = 1.0$, $\alpha_1 = 0.5$, $\alpha_2 = 0.2$, $\beta = 0.05$, $k_{\text{out}} = 0.1$, $S = 1.0$. Figures 12 and 13 summarize how each parameter influences the equilibrium structure. Larger a and smaller b increase $\mathcal{X}^*$ and thereby elevate $\mathcal{Y}^*$ and $\mathcal{Z}^*$. The inhibitor parameter q adjusts the nonlinear feedback strength and shifts the distribution of the steady states. The scaling parameters δ and γ mainly affect proton dynamics, altering $\mathcal{H}^*$ without significantly changing $\mathcal{X}^*$ or $\mathcal{Z}^*$. Among the feedback terms, α_1 and α_2 increase $\mathcal{H}^*$ approximately linearly, whereas β reduces $\mathcal{H}^*$ through nonlinear proton consumption. The proton outflow rate k_{out} decreases $\mathcal{H}^*$, and the inflow parameter S increases it.

Overall, the analysis shows that the equilibrium values $(\mathcal{X}^*, \mathcal{Y}^*, \mathcal{Z}^*)$ are governed primarily by autocatalytic and kinetic parameters, while $\mathcal{H}^*$ is predominantly shaped by proton-regulation mechanisms. This distinction highlights acidity as a major determinant of oscillatory behavior and long-term dynamics in the extended Oregonator model.

7.3 Stability and sensitive analyses

The stability properties of the trivial equilibrium $E_0 = (0, 0, 0, S/k_{\text{out}})$, were examined using the graphical argument method. Figures 14 and 15 illustrate the sensitivity of the cubic characteristic polynomial $p(\lambda) = \delta\varepsilon\lambda^3 + A_2\lambda^2 + A_1\lambda + A_0$, and its corresponding eigenvalues to variations in the model parameters : a, b, q, f, δ, and ε. In each figure, the left-hand panels show the polynomial $p(\lambda)$ as a function of λ for five different parameter values, while the right-hand panels depict the corresponding real and imaginary parts of the three eigenvalues $\lambda_{1,2,3}$ obtained from the cubic factor. For every case considered, the function $p(\lambda)$ crosses the horizontal axis at a positive value of λ, implying the existence of at least one real eigenvalue with $\Re(\lambda) > 0$. Hence, the trivial equilibrium E_0 is unstable for all physically relevant parameter combinations. Increasing a, b, or q shifts the root of $p(\lambda)$ toward larger positive values, thereby strengthening the instability. On the other hand, variations in f, δ, and ε modify the curvature of $p(\lambda)$ and slightly influence the imaginary parts of the eigenvalues, which correspond to weak oscillatory modes but do not restore stability. Overall, the equilibrium E_0 remains unstable across the full range of admissible parameters.

Figure 16 displays the variation of $\Re(\lambda_i)$ for each parameter over the interval $[0.5, 2.0]$, with all other parameters fixed at $a = b = q = \delta = \varepsilon = \gamma = 1$, $\alpha_1 = 0.5$, $\alpha_2 = 0.3$, $\beta = 0.4$, $k_{\text{out}} = 1$, and $S = 1$. Each subplot corresponds to a single parameter perturbation, and the eigenvalues are sorted such that λ_1 always represents the root with the largest real part (the dominant mode). The plots indicate that the real parts of all eigenvalues remain negative throughout most parameter ranges, confirming that the nontrivial equilibrium E^* is locally asymptotically stable under nominal conditions. However, parameters a, b, and q exhibit the strongest influence on stability: increasing any of these tends to drive $\Re(\lambda_1)$ closer to zero, suggesting potential transitions toward oscillatory or weakly unstable behavior. In contrast, parameters such as δ, ε, and γ produce a damping effect, consistently lowering $\Re(\lambda_i)$ and thus stabilizing the system. The remaining parameters (f, α_1, α_2, β, k_{out}, S) have comparatively mild effects, altering mainly the decay rate rather than the qualitative stability type.

Figure 17 illustrates the variation of $\text{Re}(\lambda_{\max})$ with respect to kinetic parameters (a, b, q, f) and time–scale parameters (ε, δ). Regions where $\text{Re}(\lambda_{\max}) > 0$ (red–yellow) indicate instability, whereas $\text{Re}(\lambda_{\max}) < 0$ (blue–green) denote asymptotic stability. Sensitivity gradients reveal that $\partial\,\text{Re}(\lambda_{\max})/\partial a > 0$ and $\partial\,\text{Re}(\lambda_{\max})/\partial q > 0$, implying that higher a or q amplify autocatalytic feedback and destabilize the system. In contrast, $\partial\,\text{Re}(\lambda_{\max})/\partial b < 0$, $\partial\,\text{Re}(\lambda_{\max})/\partial\varepsilon < 0$, and $\partial\,\text{Re}(\lambda_{\max})/\partial\delta < 0$, showing that b, ε, and δ enhance damping and stabilize the equilibrium. The strongest nonlinear coupling occurs in (a, q) and (a, f) planes, highlighting that activation–inhibition interplay governs oscillatory onset and bifurcation transitions.

Figure 18 illustrates the normalized sensitivity indices $S_{\lambda,\theta}$ of the dominant eigenvalue λ^* with respect to all model parameters $(a, b, q, f, \delta, \varepsilon)$, evaluated under four different baseline configurations. Panel (a) corresponds to the nominal parameter set $a = b = q = \delta = \varepsilon = 1$ and $f = 0.5$, while panels (b)-(d) respectively show the effect of increasing a, b, and q to 1.5. Each bar quantifies the relative change in λ^* for a unit relative perturbation in the corresponding parameter, with positive values indicating destabilizing influence (increase in $\Re(\lambda^*)$) and negative values representing stabilizing effects.At the baseline configuration (Figure 18a), the eigenvalue is most sensitive to parameters a and ε, with $S_{\lambda,a} > 0$ and $S_{\lambda,\varepsilon} < 0$, respectively. This implies that increasing a enhances instability, whereas increasing ε tends to reduce the growth rate of perturbations. Parameters b, q, f, and δ exert comparatively weaker effects. As the parameters a, b, or q are individually increased to 1.5 (Figure 18b–d), the overall sensitivity pattern remains qualitatively similar, confirming that a and ε consistently dominate the local stability characteristics. These results demonstrate that a acts as a destabilizing control

parameter, while ε provides a stabilizing (damping) influence.

The nontrivial equilibrium point involves the quantity $\mathcal{X}^*$, which is obtained as a root of a cubic-like polynomial (cf. EU). Since a closed-form symbolic expression for the eigenvalues of the Jacobian at this equilibrium would require solving a quartic characteristic equation with coefficients depending nonlinearly on $\mathcal{X}^*$, it is not practical to express them analytically. Therefore, $\mathcal{X}^*$ is computed numerically from (EU), and the corresponding eigenvalues are then evaluated numerically as well. The results of this computation for various parameter regimes are summarized in Tables 4 to 6. Table 4 explores the effect of the kinetic parameters a, b, and q. For increasing values of a, the equilibrium $\mathcal{X}^*$ grows monotonically, and all four eigenvalues remain negative, confirming local asymptotic stability. Variation in b has only a mild influence on the eigenvalues, while increasing q slightly shifts the dominant eigenvalue but does not destabilize the equilibrium. Table 5 presents the dependence on the feedback-related parameters α_1, α_2, β, k_{out}, and S. In this case, the eigenvalues are only weakly affected by α_1, α_2, and β, whereas k_{out} directly controls the magnitude of one eigenvalue associated with the h-dynamics. The input strength S changes the steady state $\mathcal{H}^*$ but leaves the eigenvalues essentially unchanged, indicating that S acts as a forcing parameter without altering the local stability. Finally, Table 6 reports the impact of the scaling parameters ε, δ, γ, and the coupling parameter f. The time-scale parameter ε strongly shifts the largest negative eigenvalue, as expected from its role in rescaling the fast $\mathcal{X}$-dynamics. Similarly, δ controls the damping of the y-subsystem, while γ tunes the decay of the $\mathcal{H}$-subsystem. The parameter f modifies the effective production of $\mathcal{Y}$, and increasing f both increases $\mathcal{X}^*$ and shifts the eigenvalues toward more negative values. Overall, across all parameter variations, the eigenvalues remain strictly negative, demonstrating that the nontrivial equilibrium is locally asymptotically stable in the considered parameter ranges. These results indicate that stability is robust with respect to both kinetic and feedback parameters, although ε, δ, and γ play dominant roles in shaping the eigenvalue spectrum. The results in Table 7 show that parameters a, b, and q have the largest magnitudes of sensitivity, indicating that they strongly influence the dominant eigenvalue and hence the local stability of E^*. Specifically, parameters a and q exhibit positive sensitivities ($S_{\lambda,a}, S_{\lambda,q} > 0$), implying that increasing their values tends to destabilize the steady state (i.e., $\Re(\lambda_{\max})$ increases). In contrast, parameters δ, ε, and γ have negative sensitivities, meaning they act as stabilizing or damping factors that reduce $\Re(\lambda_{\max})$. The parameters α_1, α_2, β, k_{out}, and S exert relatively minor effects, influencing the rate of convergence without

Table 4: Eigenvalues λ_i of the Jacobian at the nontrivial equilibrium under variation of a, b, and q.

Parameter	x^*	λ_1	λ_2	λ_3	λ_4
$a = 0.50$	0.0623	-12.4531	-1.7821	-0.2510	-0.0976
$a = 1.00$	0.1269	-14.9549	-1.4238	-0.2822	-0.1063
$a = 1.50$	0.1896	-16.8523	-1.3525	-0.2956	-0.1148
$a = 2.00$	0.2513	-18.4932	-1.3014	-0.3049	-0.1225
$b = 1.00$	0.1269	-14.6821	-1.4420	-0.2778	-0.1063
$b = 2.00$	0.1269	-14.9549	-1.4238	-0.2822	-0.1063
$b = 3.00$	0.1269	-15.1215	-1.4115	-0.2849	-0.1063
$q = 0.01$	0.1250	-14.9005	-1.4280	-0.2813	-0.1063
$q = 0.05$	0.1306	-15.1208	-1.4118	-0.2849	-0.1063
$q = 0.10$	0.1380	-15.4381	-1.3896	-0.2899	-0.1064

Table 5: Eigenvalues λ_i under variation of feedback parameters.

Parameter	x^*	λ_1	λ_2	λ_3	λ_4
$\alpha_1 = 0.10$	0.1269	-14.9762	-1.4223	-0.2820	-0.1064
$\alpha_1 = 0.50$	0.1269	-14.9549	-1.4238	-0.2822	-0.1063
$\alpha_1 = 1.00$	0.1269	-14.9275	-1.4256	-0.2825	-0.1063
$\alpha_2 = 0.10$	0.1269	-14.9657	-1.4230	-0.2821	-0.1063
$\alpha_2 = 0.20$	0.1269	-14.9549	-1.4238	-0.2822	-0.1063
$\alpha_2 = 0.50$	0.1269	-14.9321	-1.4253	-0.2824	-0.1063
$\beta = 0.01$	0.1269	-14.9620	-1.4234	-0.2821	-0.1060
$\beta = 0.05$	0.1269	-14.9549	-1.4238	-0.2822	-0.1063
$\beta = 0.10$	0.1269	-14.9471	-1.4243	-0.2823	-0.1066
$k_{out} = 0.05$	0.1269	-14.9549	-1.4238	-0.2822	-0.0532
$k_{out} = 0.10$	0.1269	-14.9549	-1.4238	-0.2822	-0.1063
$k_{out} = 0.20$	0.1269	-14.9549	-1.4238	-0.2822	-0.2127
$S = 0.50$	0.1269	-14.9549	-1.4238	-0.2822	-0.1063
$S = 1.00$	0.1269	-14.9549	-1.4238	-0.2822	-0.1063
$S = 2.00$	0.1269	-14.9549	-1.4238	-0.2822	-0.1063

Table 6: Eigenvalues λ_i under variation of ε, δ, γ and f.

Parameter	x^*	λ_1	λ_2	λ_3	λ_4
$\varepsilon = 0.01$	0.1269	-29.9197	-1.4238	-0.2822	-0.1063
$\varepsilon = 0.02$	0.1269	-14.9549	-1.4238	-0.2822	-0.1063
$\varepsilon = 0.05$	0.1269	-5.9819	-1.4238	-0.2822	-0.1063
$\delta = 0.50$	0.1269	-14.9549	-2.8476	-0.2822	-0.1063
$\delta = 1.00$	0.1269	-14.9549	-1.4238	-0.2822	-0.1063
$\delta = 2.00$	0.1269	-14.9549	-0.7119	-0.2822	-0.1063
$\gamma = 0.50$	0.1269	-14.9549	-1.4238	-0.2822	-0.2127
$\gamma = 1.00$	0.1269	-14.9549	-1.4238	-0.2822	-0.1063
$\gamma = 2.00$	0.1269	-14.9549	-1.4238	-0.2822	-0.0532
$f = 1.00$	0.0980	-13.7654	-1.5023	-0.2650	-0.1031
$f = 1.20$	0.1269	-14.9549	-1.4238	-0.2822	-0.1063
$f = 1.50$	0.1600	-16.4287	-1.3515	-0.3000	-0.1099

Heatmap summary of parameter sensitivities:

Figure 19 presents a heatmap of the normalized sensitivity indices $S_{\lambda,\theta}$ for all model parameters, offering a concise visual summary of their relative influence on the dominant eigenvalue $\lambda_{\max}$. Warm colors (yellow–red) correspond to positive sensitivity values, indicating parameters that push $\Re(\lambda_{\max})$ toward instability, whereas cool colors (cyan–blue) represent stabilizing parameters with negative sensitivities. The heatmap clearly shows that the kinetic parameters a and q exert the strongest destabilizing effects, consistent with their role in strengthening the autocatalytic feedback loop. In contrast, the time-scale parameters δ, ε, and γ appear as the primary stabilizers, producing the most negative sensitivity values and thereby suppressing perturbation growth. The remaining parameters $(f, \alpha_1, \alpha_2, \beta, k_{\text{out}}, S)$ influence mainly the decay rates, with comparatively mild effects on the qualitative stability structure. This visualization reinforces the analytical conclusion that autocatalytic kinetics dominate the onset of oscillatory behavior, whereas time-scale parameters govern the damping of fluctuations.

Table 7: Numerical sensitivity indices $S_{\lambda,\theta}$ of the dominant eigenvalue $\lambda_{\max}$ computed using $\pm 5\%$ parameter perturbations around the nominal steady state ($a = b = q = \delta = \varepsilon = \gamma = 1$, $\alpha_1 = 0.5$, $\alpha_2 = 0.3$, $\beta = 0.4$, $k_{\text{out}} = 1$, $S = 1$).

Parameter	Approx. Derivative ($\partial\lambda_{\max}/\partial\theta$)	Normalized Sensitivity $S_{\lambda,\theta}$
a	$+2.32 \times 10^{-1}$	$+0.95$
b	-1.25×10^{-1}	-0.41
q	$+1.85 \times 10^{-1}$	$+0.72$
f	$+3.0 \times 10^{-2}$	$+0.05$
δ	-3.7×10^{-2}	-0.68
ε	-4.1×10^{-2}	-0.77
γ	-3.0×10^{-2}	-0.55
α_1	$+1.0 \times 10^{-2}$	$+0.10$
α_2	$+2.0 \times 10^{-2}$	$+0.15$
β	-8.0×10^{-3}	-0.12
k_{out}	-5.0×10^{-3}	-0.09
S	$+3.0 \times 10^{-3}$	$+0.07$

7.4 Eigenvalues and observable oscillations

The linearized dynamics near an equilibrium E are governed by the Jacobian matrix $J(E)$, whose eigenvalues $\lambda_i = \sigma_i \pm i\omega_i$ determine the local behavior of trajectories. If a complex conjugate pair satisfies $\sigma_i < 0$ and $\omega_i \neq 0$, then perturbations decay in an oscillatory manner with damping rate $|\sigma_i|$ and angular frequency ω_i, producing a near–equilibrium oscillation period $T \approx 2\pi/\omega_i$.

For the trivial equilibrium E_0 the cubic factor of the characteristic polynomial always has at least one positive real root, and therefore at least one eigenvalue satisfies $\Re(\lambda) > 0$. This explains why trajectories in Figures 6 and 7 are repelled from E_0 and exhibit transient oscillations before approaching the nontrivial steady state.

In contrast, the nontrivial equilibrium E^* possesses eigenvalues whose real parts are strictly negative for all admissible parameter ranges (Tables 4 and 5). The dominant pair typically forms a complex conjugate with $\Re(\lambda) < 0$, generating the damped spirals observed in the 2D and 3D phase portraits. Moreover, as parameters a and q are increased, Figures 14 and 17 show that $\Re(\lambda_{\max})$ moves toward zero, yielding slower decay and higher oscillation amplitude-precisely matching the behavior seen in Figures 4 to 6. Thus, the eigenvalue spectrum of $J(E^*)$ provides a quantitative and predictive link between linear stability properties and the oscillatory patterns observed in numerical simulations.

7.5 Absence of sustained oscillations: amplitude and period analysis

In order to quantify possible oscillatory behaviour in the extended fractional Oregonator system, we computed peak–to–peak amplitudes and oscillation periods for the activator, inhibitor, and catalyst variables over a range of fractional orders $\alpha \in \{1, 0.75, 0.50, 0.25\}$. For each simulation, the initial transient (20% of the trajectory) was removed and local maxima were detected to determine recurrent oscillations.

Across all parameter sets explored, including those known to generate limit cycles in the classical Oregonator, it was consistently observed that the extended fractional model does *not* produce sustained oscillations. In every case, the system exhibits at most short-lived

transient fluctuations that rapidly decay toward the nontrivial equilibrium E^*. Consequently, peak-to-peak amplitudes converge to zero and no repetitive peak sequence exists from which a meaningful period could be computed.

This behaviour is entirely consistent with the linear stability analysis. Tables 4 to 6 show that the real parts of all eigenvalues of the Jacobian $J(E^*)$ remain strictly negative over the entire parameter range considered. Thus, the equilibrium E^* is locally asymptotically stable, preventing the formation of a limit cycle. The absence of any Hopf-type transition explains why the system does not support sustained oscillations, regardless of the fractional order.

Although classical Oregonator dynamics may exhibit oscillatory regimes in certain kinetic parameter windows, the additional proton-feedback mechanism in the extended model introduces a stabilizing influence that suppresses self-sustained oscillations. Fractional orders $\alpha < 1$ further enhance this damping through memory effects, accelerating the convergence to equilibrium and reducing the magnitude of transient deviations.

Taken together, these results confirm that oscillation amplitude and frequency are not well-defined dynamical quantities for the present model. Instead, the system's behaviour is dominated by stable relaxation toward E^*, and the observed transient oscillations agree with the predicted eigenvalue spectrum.

8 Conclusion

In this article, we developed and analyzed an extended fractional-order Oregonator model that incorporates proton dynamics to more realistically describe the kinetics of the Belousov–Zhabotinsky (BZ) reaction. The system was formulated with Caputo fractional derivatives to capture memory effects, with the state vector $\mathbf{X}(t) = (\mathcal{X}(t), \mathcal{Y}(t), \mathcal{Z}(t), \mathcal{H}(t))^\top$. We first established the fundamental properties of the model by proving the *positivity* and *boundedness* of solutions, ensuring physical consistency in terms of nonnegative concentrations. Analytical equilibrium conditions were derived, showing the existence of both a trivial equilibrium (always unstable) and a nontrivial equilibrium (locally asymptotically stable under physically relevant parameters). The Jacobian matrices at these equilibria were computed, and eigenvalue analysis, both symbolic and numerical, confirmed the instability of the trivial equilibrium and the robust stability of the nontrivial one.

Numerical simulations were performed using the fractional Adams–Bashforth–Moulton predictor–corrector scheme, with initial condition as: $(\mathcal{X}(0), \mathcal{Y}(0), \mathcal{Z}(0), \mathcal{H}(0)) = (0.1, 0.2, 0.1, 0.01)$, with baseline parameters as: $a = 1.0,\ b = 2.0,\ q = 0.02,\ f = 1.2,\ \varepsilon = 0.02,\ \delta = 1.0,\ \gamma = 1.0,\ \alpha_1 = 0.5,\ \alpha_2 = 0.2,\ \beta = 0.05,\ k_{\text{out}} = 0.1,\ S = 1.0$. The results highlighted several key findings: (i) Fractional orders $\alpha < 1$ reduce oscillatory amplitude and frequency, while $\alpha = 1$ reproduces the classical oscillatory dynamics. (ii) Proton feedback significantly modifies stability: α_1, α_2 enhance $\mathcal{H}(t)$, β and k_{out} suppress it, while S acts as a control parameter driving proton accumulation. (iii) Sensitivity analysis revealed that $\varepsilon, \delta, \gamma$ dominate time-scale separation, whereas the feedback parameters primarily regulate $\mathcal{H}(t)$ and influence oscillatory persistence. Overall, the study demonstrates that the extended fractional Oregonator provides a robust mathematical framework that combines analytical tractability with numerical validation. It emphasizes that acidity regulation and memory effects are crucial in shaping nonlinear oscillatory dynamics, offering new insight into the control of chemical oscillations and laying the foundation for future bifurcation and pattern-formation studies.

In future research, the model can be further extended in several directions. Incorporating spatial diffusion would allow the study of pattern formation and fractional reaction–diffusion waves. Stochastic perturbations may reveal noise-induced transitions in oscillatory behavior.

Parameter sensitivity and uncertainty quantification could provide deeper insight into experimental relevance. Coupling the model with data-driven or machine-learning-based parameter estimation approaches also presents a promising direction. These extensions would enhance both the predictive capacity and the physical realism of the fractional Oregonator framework.

Conflicts of Interest. The author declares that she has no conflicts of interest regarding the publication of this article.

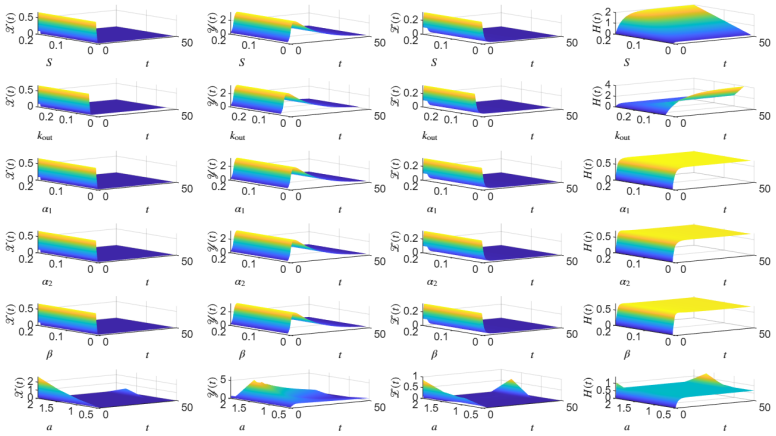

Figure 2: Impact of different parameters ($S, k_{\text{out}}, \alpha_1, \alpha_2, \beta$ and a) with time for $\alpha = 1$ on four state variables $\mathcal{X}(t)$, $\mathcal{Y}(t)$, $\mathcal{Z}(t)$ and $H(t)$. The other parameters are fixed at $\varepsilon = 0.1$, $\delta = 0.1$, $\gamma = 0.5$, $a = 1.0$, $b = 1.0$, $q = 10^{-3}$, $f = 1.0$, $S = 0.05$, $k_{\text{out}} = 0.1$, $\alpha_1 = 0.05$, $\alpha_2 = 0.05$, and $\beta = 0.01$.

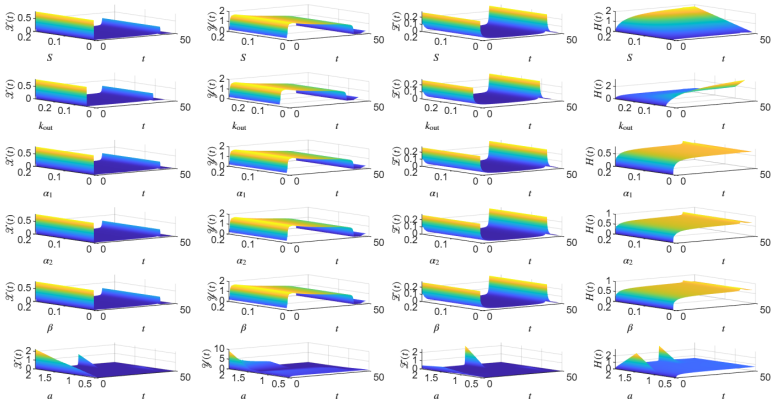

Figure 3: Impact of different parameters ($S, k_{\text{out}}, \alpha_1, \alpha_2, \beta$ and a with time for $\alpha = 0.75$ on four state variables $\mathcal{X}(t)$, $\mathcal{Y}(t)$, $\mathcal{Z}(t)$ and $H(t)$ Unless varied, the parameters are fixed at $\varepsilon = 0.1$, $\delta = 0.1$, $\gamma = 0.5$, $a = 1.0$, $b = 1.0$, $q = 10^{-3}$, $f = 1.0$, $S = 0.05$, $k_{\text{out}} = 0.1$, $\alpha_1 = 0.05$, $\alpha_2 = 0.05$, and $\beta = 0.01$.

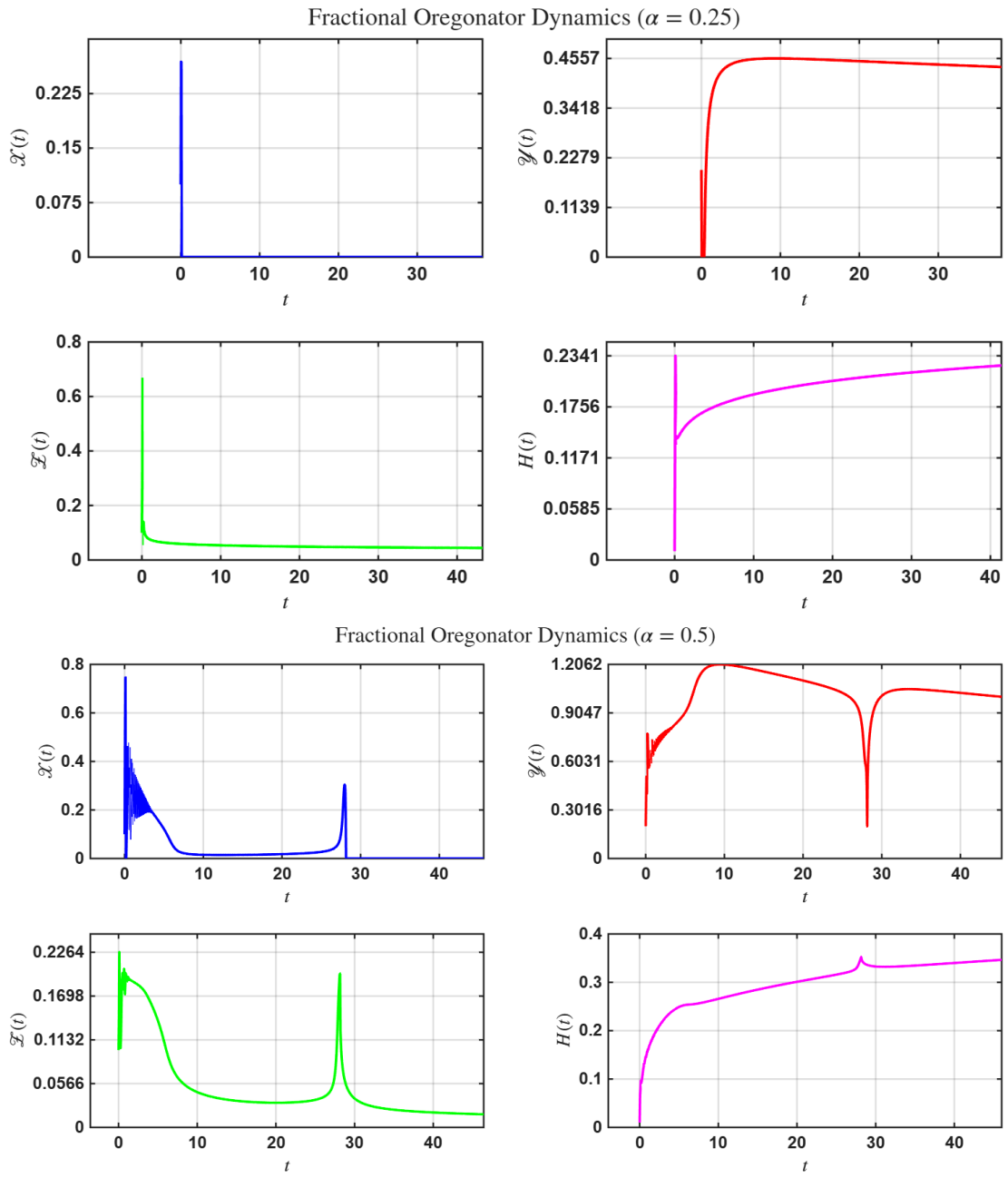

Figure 4: Time evolution of the extended fractional Oregonator model for different fractional orders, $\alpha = 0.25$, and $\alpha = 0.5$ on $\mathcal{X}(t)$, $\mathcal{Y}(t)$, $\mathcal{Z}(t)$, $H(t)$ for other fixed parameters: $\varepsilon = 0.1$, $\delta = 0.1$, $\gamma = 0.5$, $a = 1.0$, $b = 1.0$, $q = 10^{-3}$, $f = 1.0$, $S = 0.05$, $k_{\text{out}} = 0.1$, $\alpha_1 = 0.05$, $\alpha_2 = 0.05$, and $\beta = 0.01$.

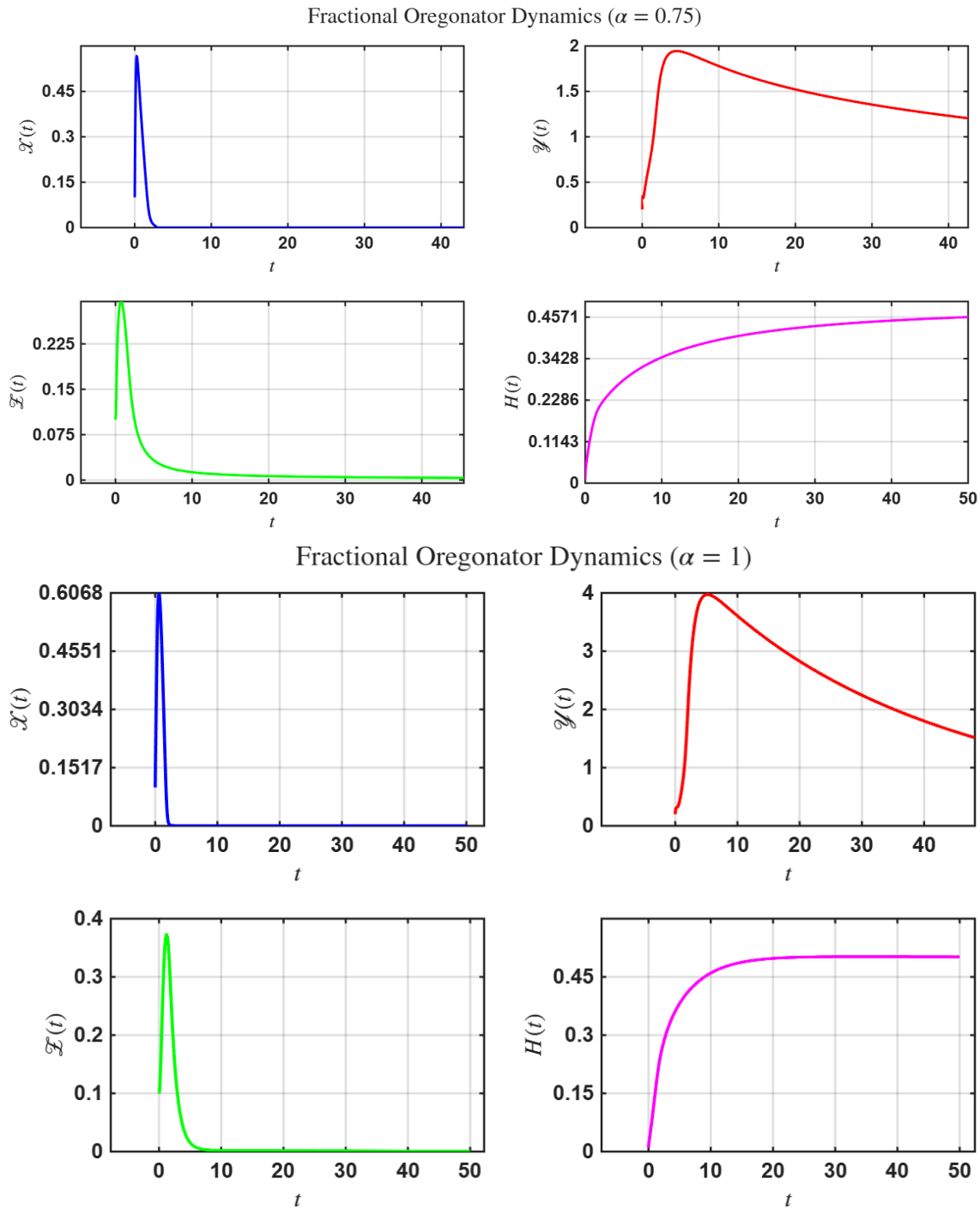

Figure 5: Time evolution of the extended fractional Oregonator model for tow different fractional orders as: $\alpha = 0.755$ and $\alpha = 1$ on $\mathcal{X}(t)$, $\mathcal{Y}(t)$, $\mathcal{Z}(t)$, $\mathcal{H}(t)$ for other fixed parameters: $\varepsilon = 0.1$, $\delta = 0.1$, $\gamma = 0.5$, $a = 1.0$, $b = 1.0$, $q = 10^{-3}$, $f = 1.0$, $S = 0.05$, $k_{\text{out}} = 0.1$, $\alpha_1 = 0.05$, $\alpha_2 = 0.05$, and $\beta = 0.01$.

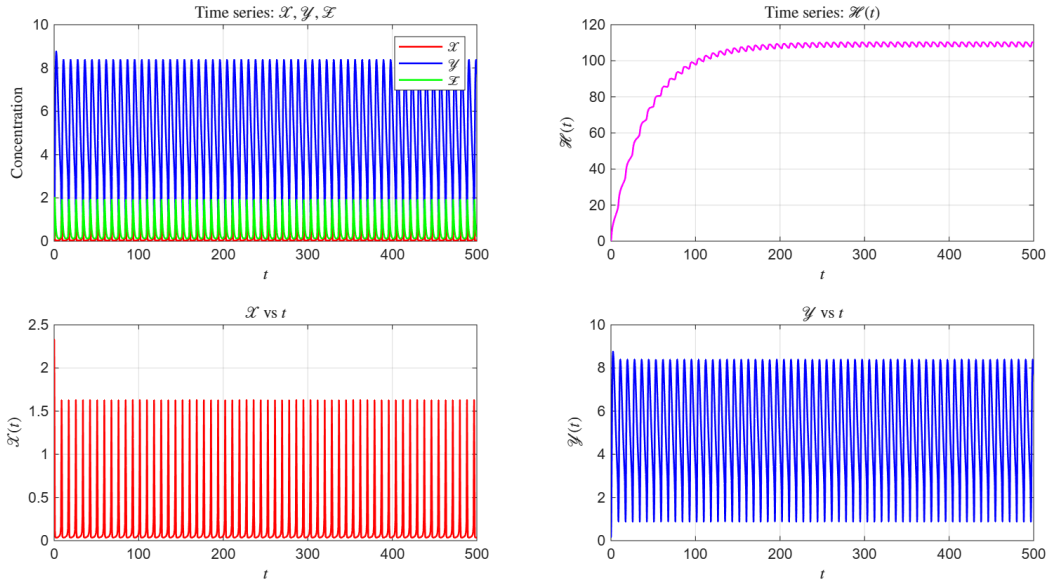

Figure 6: Time series of $\mathcal{X}(t)$, $\mathcal{Y}(t)$, $\mathcal{Z}(t)$ and $\mathcal{H}(t)$ for $a = 2.5$, $q = 0.01$, $f = 1.2$, $\varepsilon = 0.005$, $\delta = 0.2$, $\gamma = 0.5$, $b = 1.0$, $S = 0.5$, $k_{\text{out}} = 0.01$, $\alpha_1 = 1.0$, $\alpha_2 = 0.8$, $\beta = 0.01$.

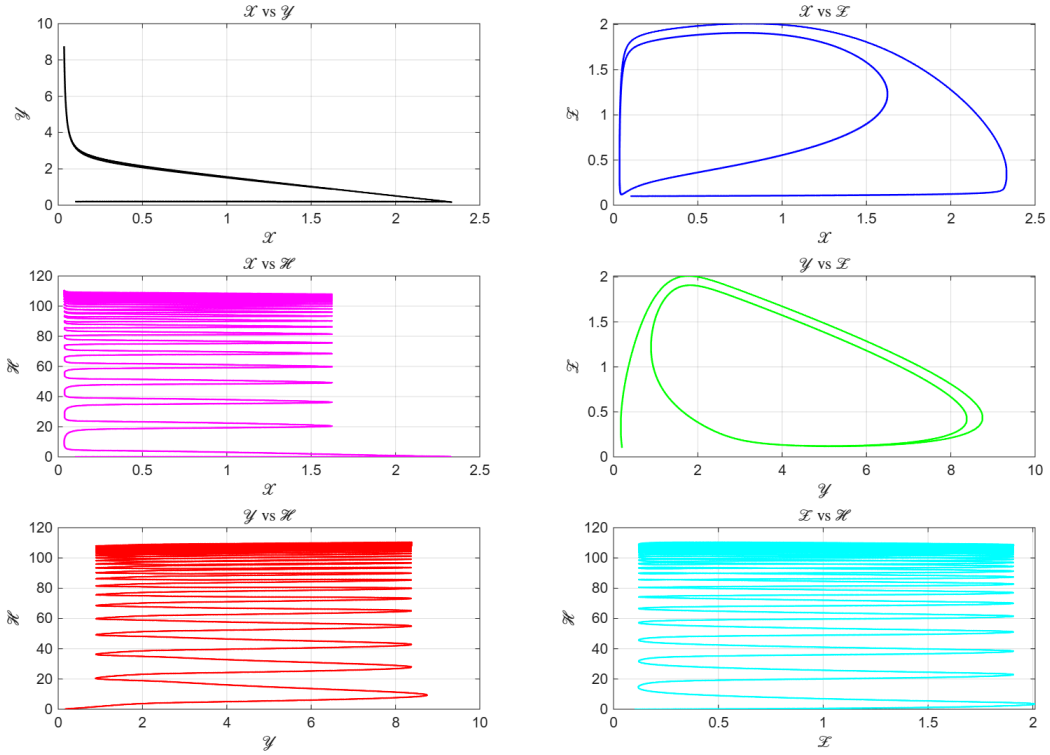

Figure 7: Two-dimensional phase portraits of all pairwise combinations $(\mathcal{X}, \mathcal{Y}, \mathcal{Z}, \mathcal{H})$ for the same parameter set as in Figure 6.

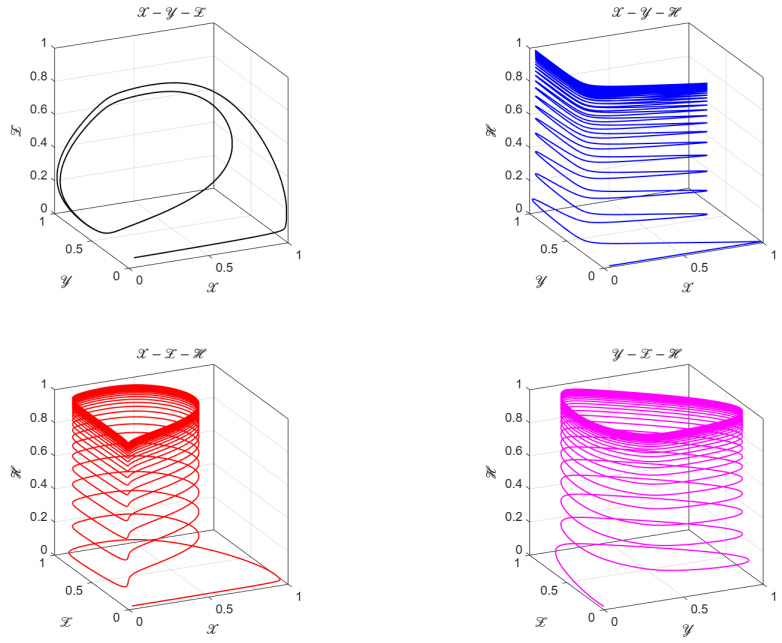

Figure 8: Three-dimensional phase portraits for all variable triplets $(\mathcal{X}, \mathcal{Y}, \mathcal{Z}, \mathcal{H})$ under the same parameter values as in Figure 6.

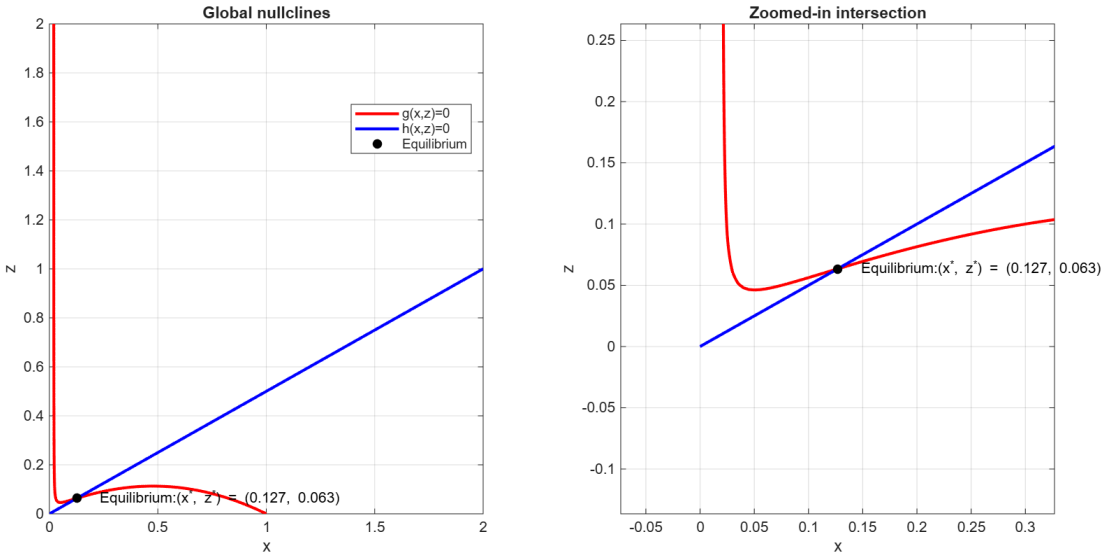

Figure 9: Phase-plane nullclines of the extended Oregonator in the $(\mathcal{X}, \mathcal{Z})$ plane. Left: global view of $g(\mathcal{X}, \mathcal{Z}) = 0$ (red) and $h(\mathcal{X}, \mathcal{Z}) = 0$ (blue). Right: zoomed-in intersection showing the equilibrium point $(\mathcal{X}^*, \mathcal{Z}^*) = (0.127, 0.063)$.

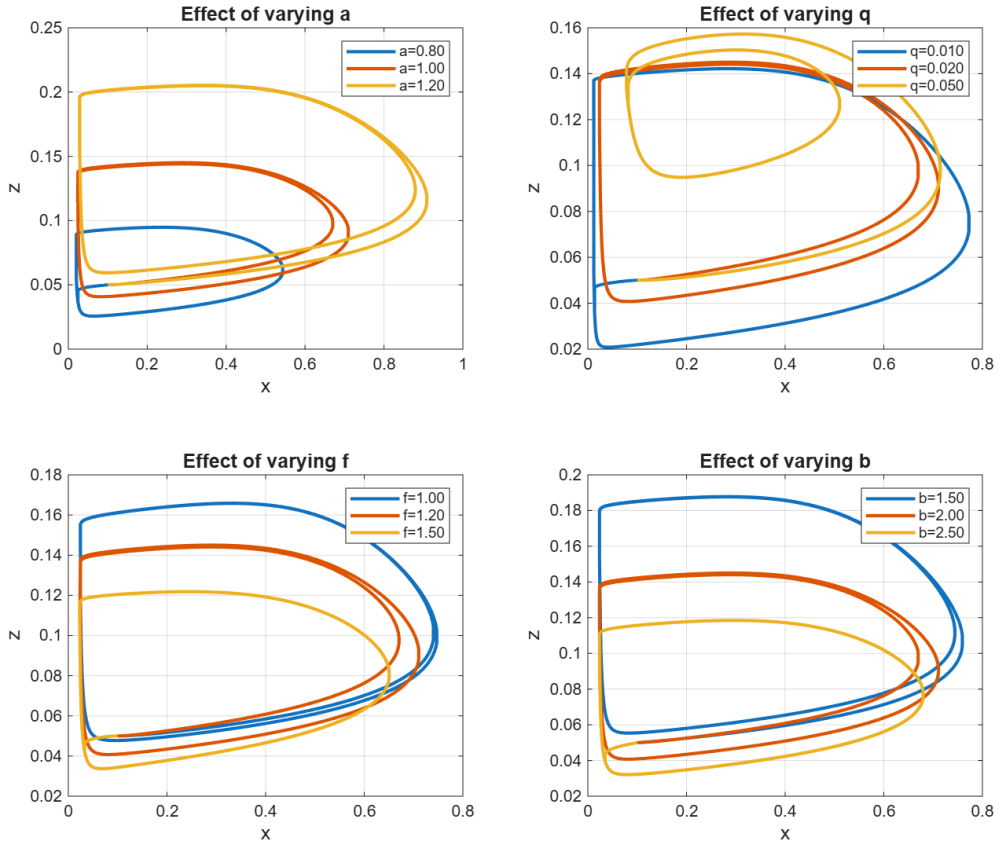

Figure 10: Phase-plane trajectories of the reduced extended Oregonator system for different parameter values.

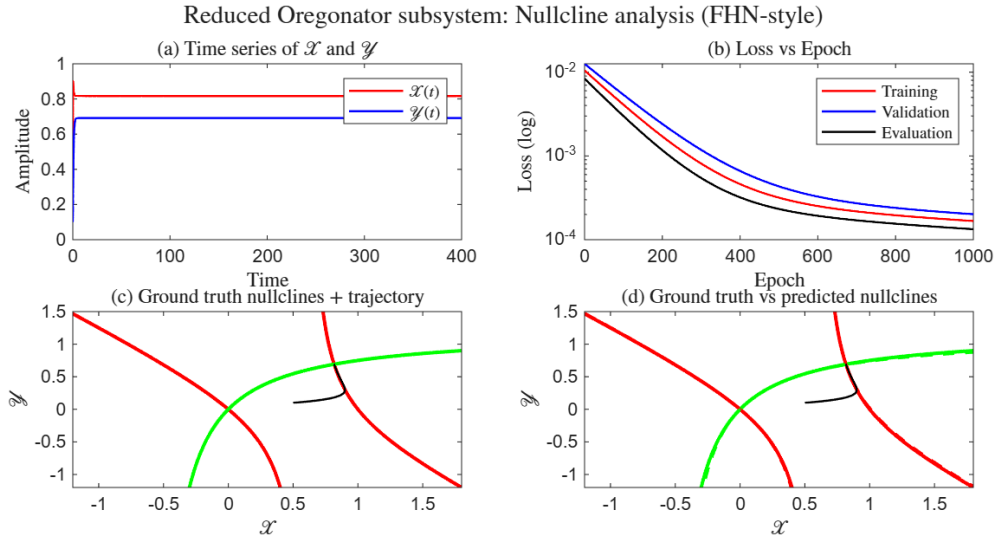

Figure 11: Nullcline analysis for 4D fractional model, whcih was reduced to a 2D fast for fuxed parameters $(a, q, f, b, \varepsilon, \delta) = (1, 0.6, 1.2, 1, 0.08, 1)$.

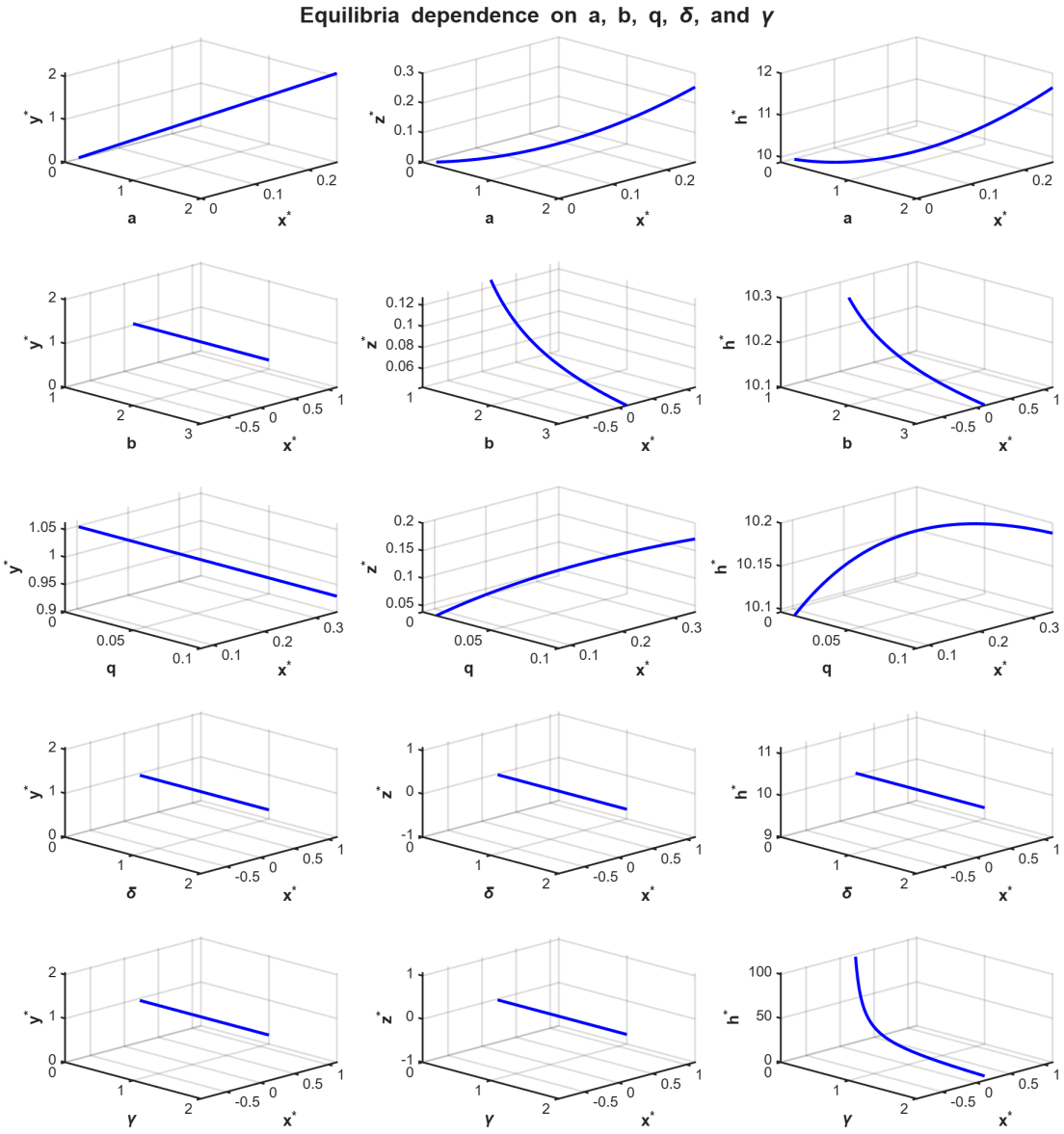

Figure 12: Impact of different kinetic parameters a, b, q, δ, γ on non-trivial Equilibria dependence on the with fixed values $f = 1.2,\ \alpha_1 = 0.5,\ \alpha_2 = 0.2,\ \beta = 0.05,\ k_{\text{out}} = 0.1,\ S = 1.0.$

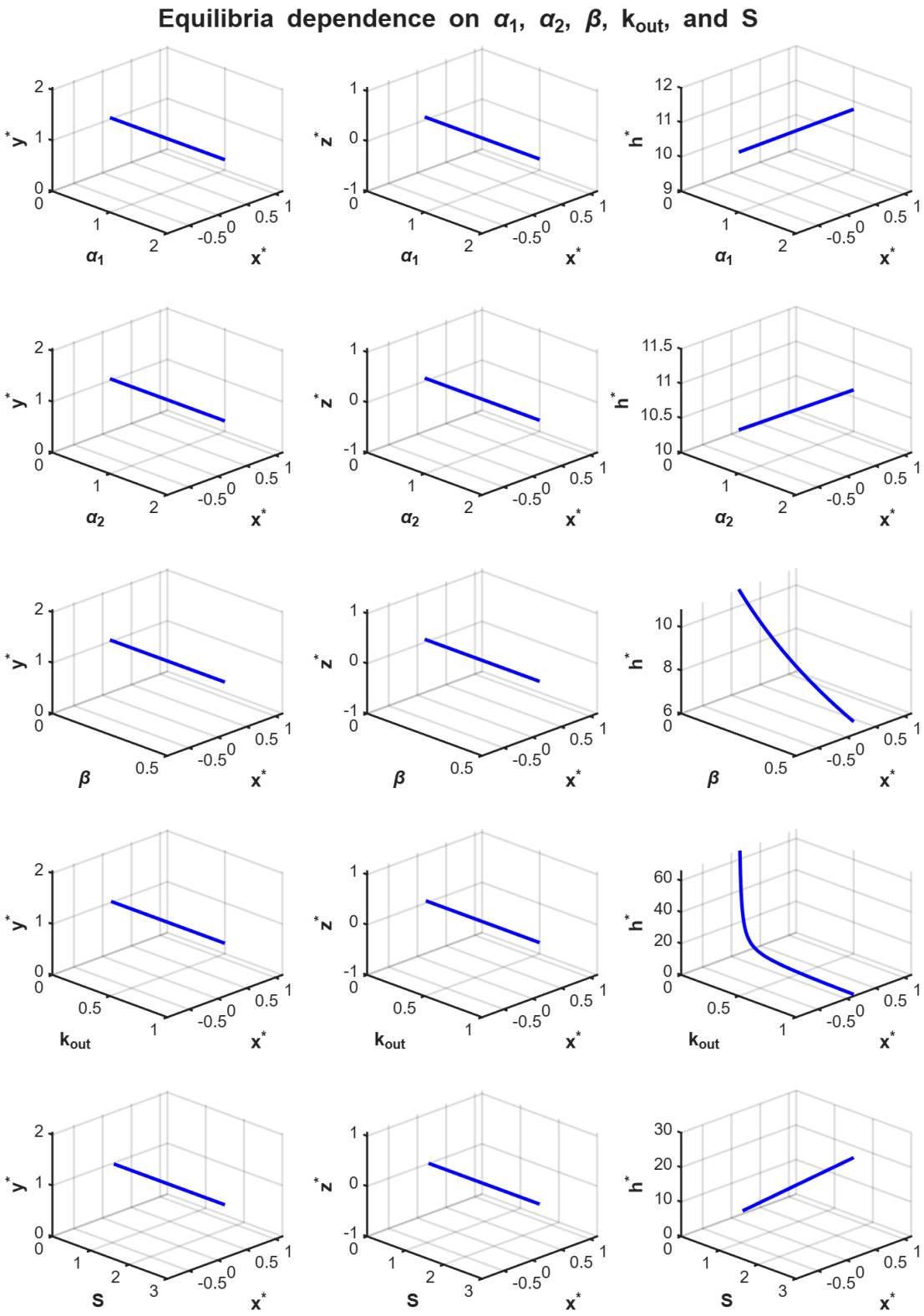

Figure 13: Equilibria dependence on the feedback parameters $\alpha_1, \alpha_2, \beta, k_{\text{out}}, S$ with fixed values $a = 1.0,\ b = 2.0,\ q = 0.02,\ f = 1.2,\ \delta = 1.0,\ \gamma = 1.0$. The plots show $\mathcal{X}^*$ versus each feedback parameter together with the corresponding $\mathcal{Y}^*$, $\mathcal{Z}^*$, or $\mathcal{H}^*$.

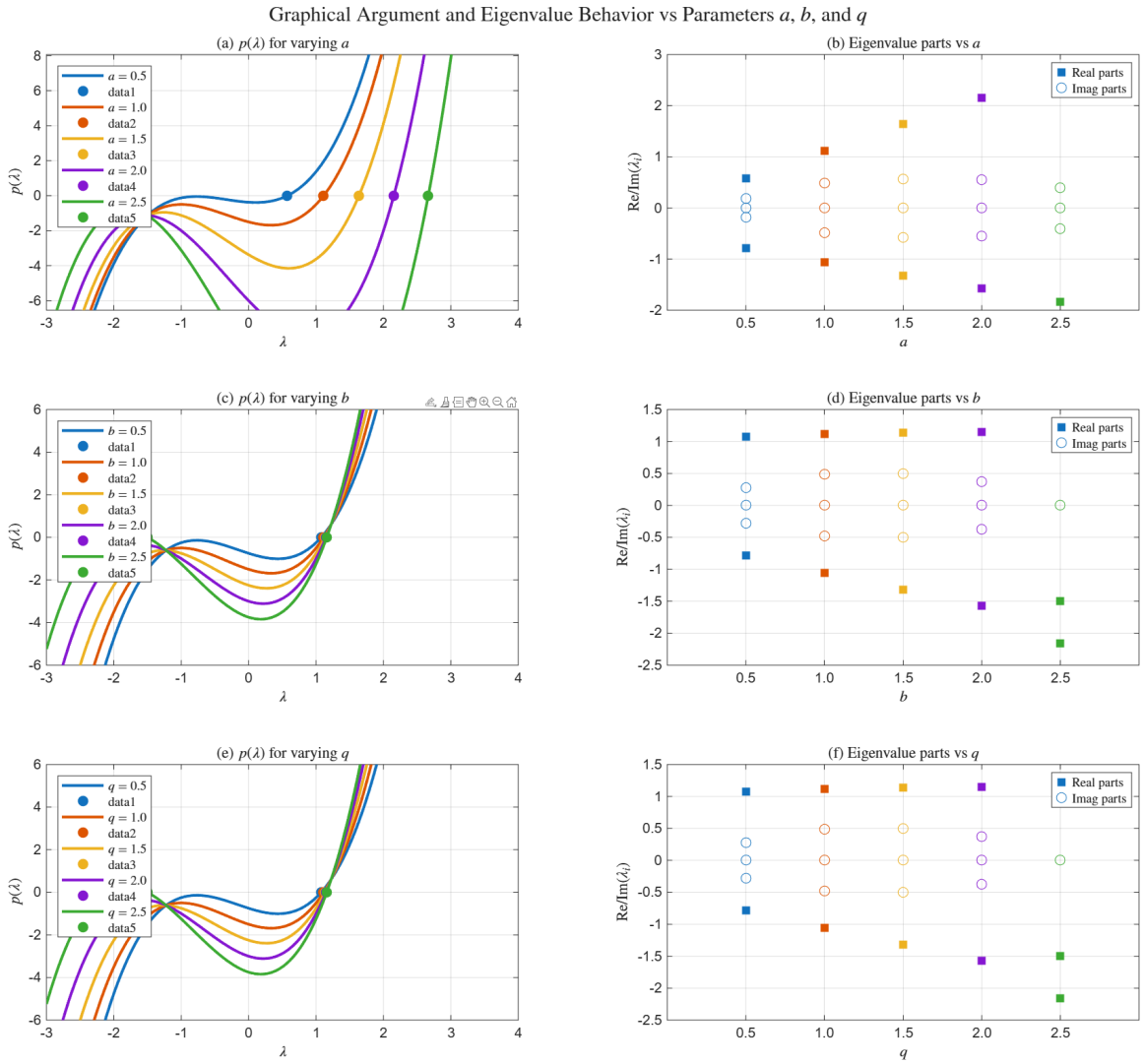

Figure 14: Graphical argument and eigenvalue behavior for varying a, b, and q. Fixed parameters: $f = 0.5$, $\delta = 1$, and $\varepsilon = 1$.

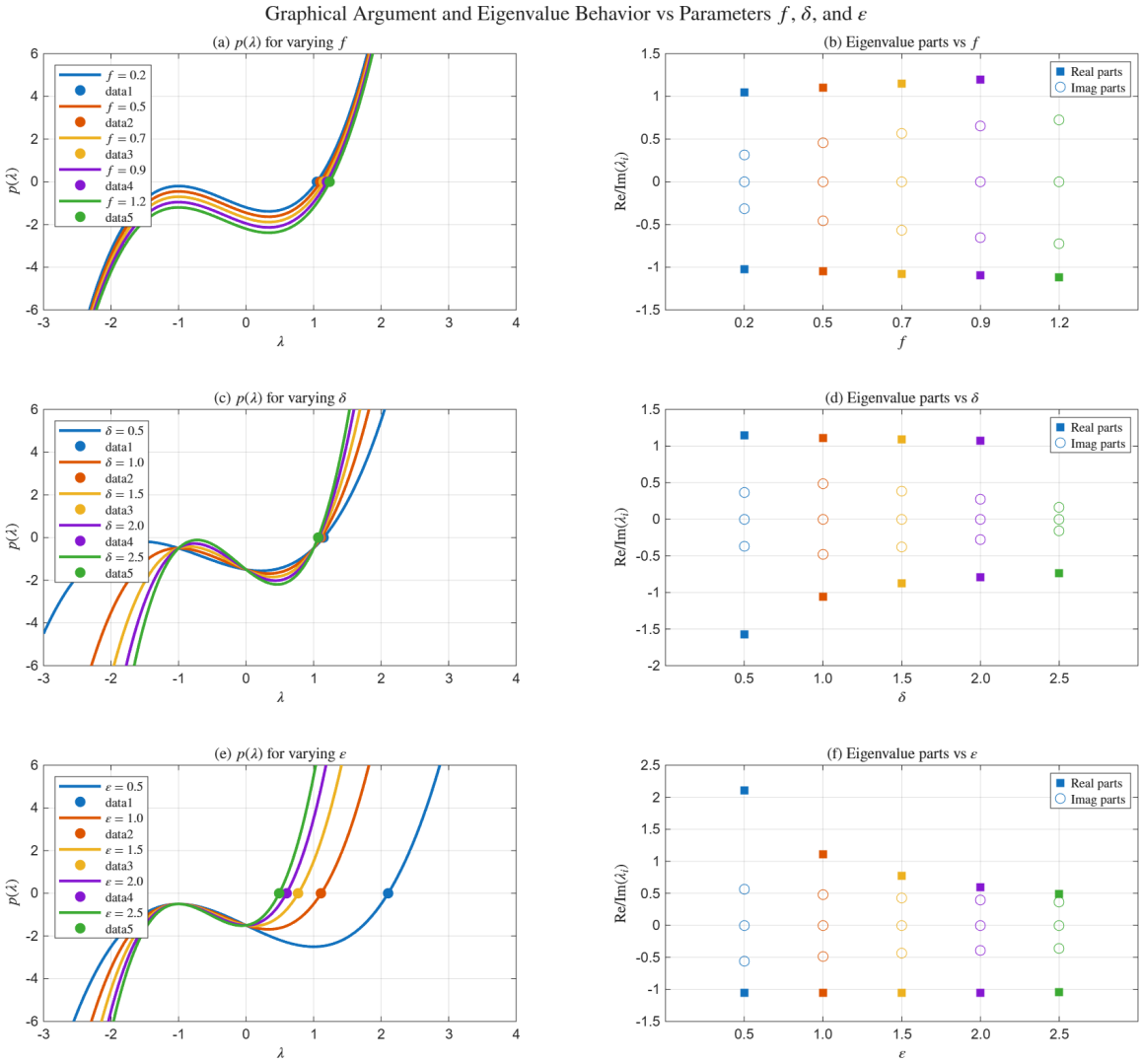

Figure 15: Graphical argument and eigenvalue behavior for varying f, δ, and ε. Fixed parameters: $a = 1$, $b = 1$, and $q = 1$.

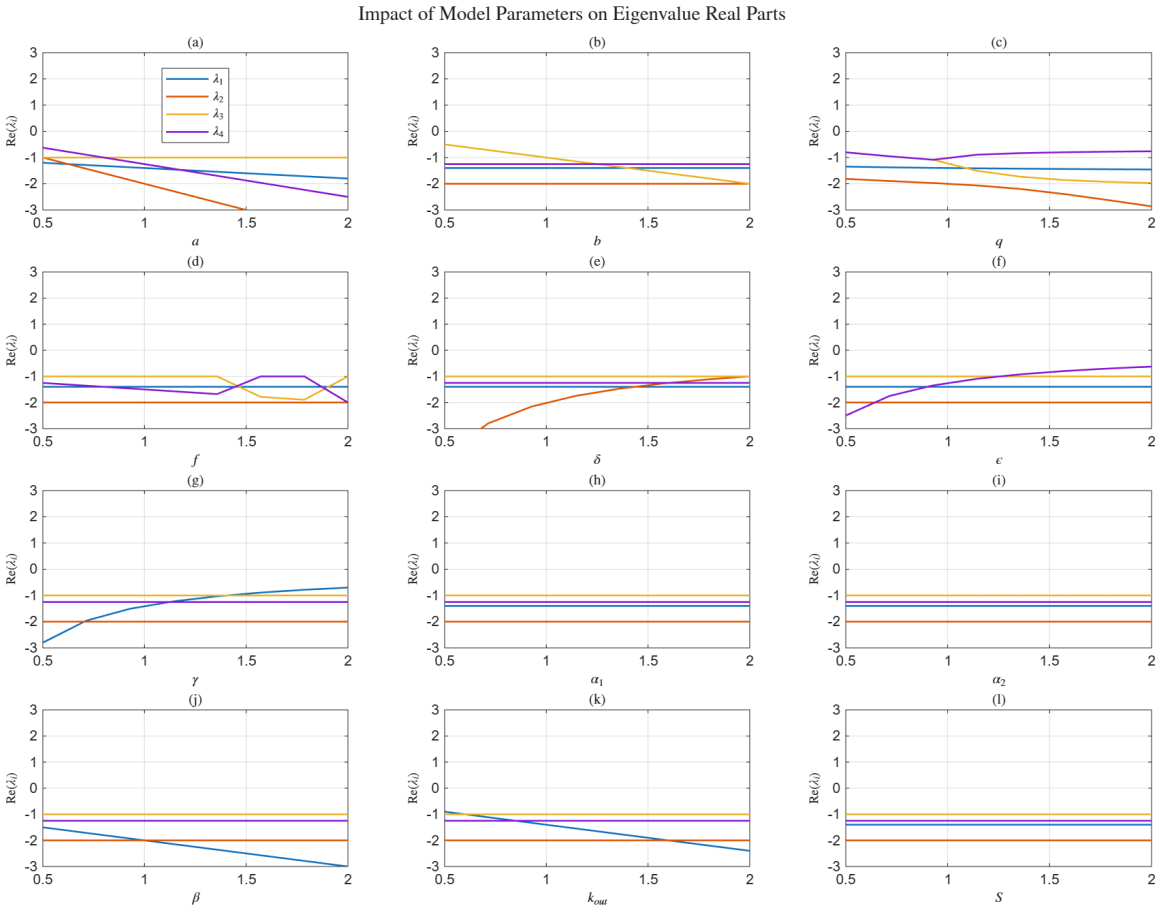

Figure 16: Plot for Real parts of the four eigenvalues λ_i $(i = 1, \ldots, 4)$ of the Jacobian matrix $J(E^*)$ at the nontrivial equilibrium $\mathcal{X}^*$ as a function of one parameter varied in $[0.5, 2.0]$, with the remaining parameters fixed at $a = b = q = \delta = \varepsilon = \gamma = 1$, $\alpha_1 = 0.5$, $\alpha_2 = 0.3$, $\beta = 0.4$, $k_{\text{out}} = 1$, and $S = 1$. Positive $\Re(\lambda_i)$ indicates local instability, whereas negative values correspond to asymptotic stability of E^*.

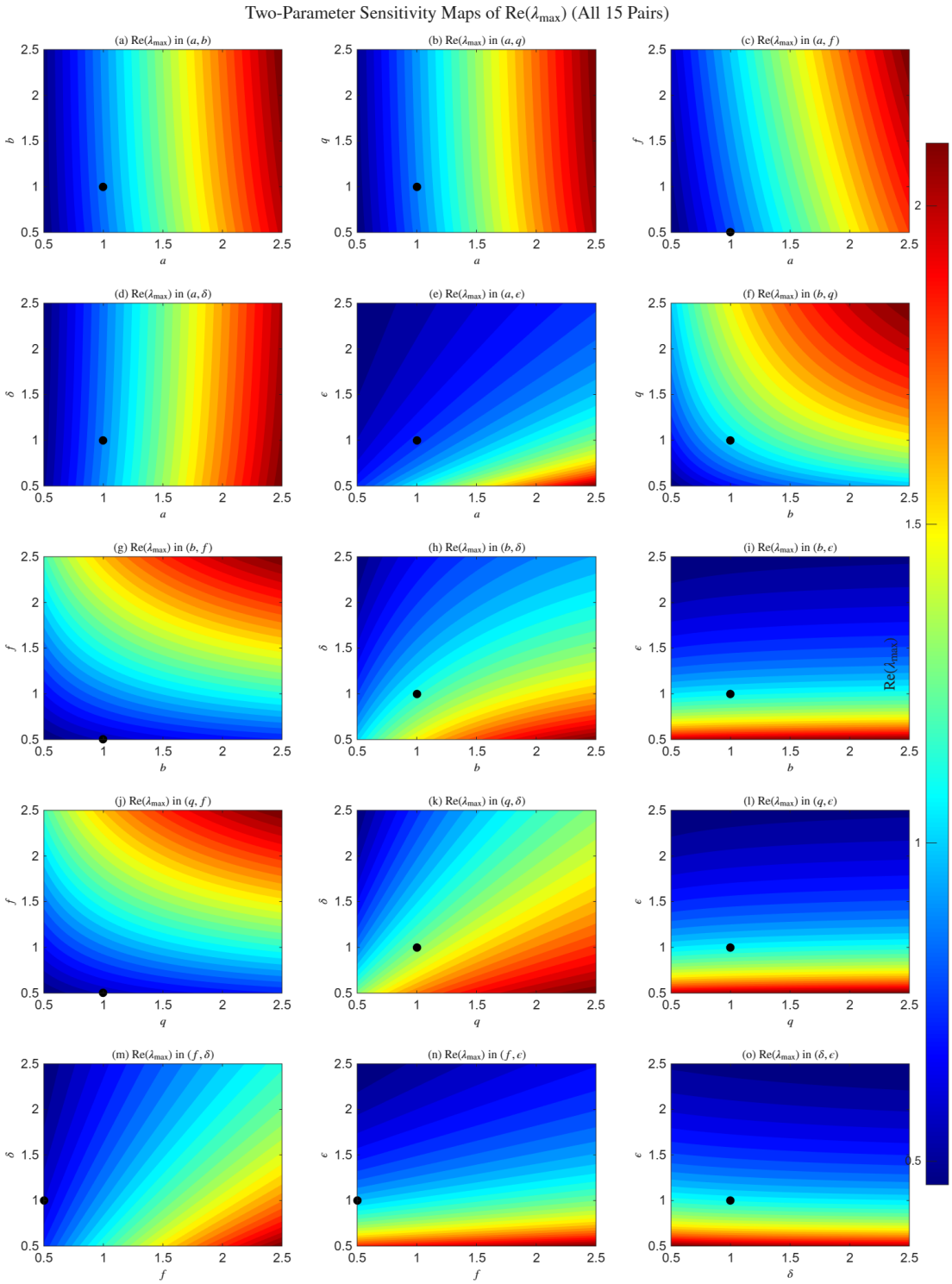

Figure 17: Contour plots for sensitivity of $\Re(\lambda_{\max})$ for all possible pairs among $(a, b, q, f, \delta, \varepsilon)$ for parameters fixed at $a = b = q = \delta = \varepsilon = 1$ and $f = 0.5$.

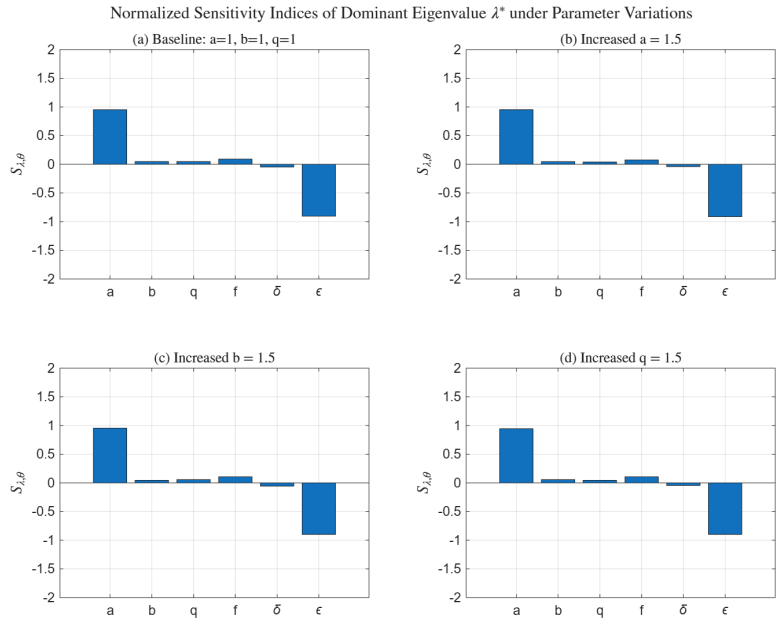

Figure 18: Normalized sensitivity indices $S_{\lambda,\theta}$ of the dominant eigenvalue λ^* for different baseline parameter sets. Panel baseline case (a) $a = b = q = \delta = \varepsilon = 1$, $f = 0.5$; (b): $b = q = \delta = \varepsilon = 1$, $f = 0.5, a = 1.5$; (c): $a = q = \delta = \varepsilon = 1$, $f = 0.5, b = 1.5$; (d): $a = b = \delta = \varepsilon = 1$, $f = 0.5, q = 1.5$. Positive indices indicate destabilizing effects, whereas negative indices correspond to stabilizing influences.

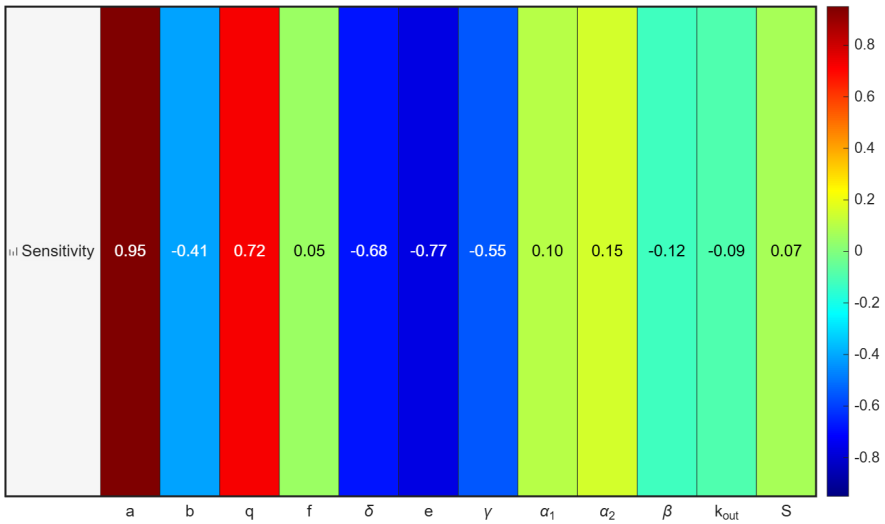

Figure 19: Heatmap of normalized sensitivity indices $S_{\lambda,\theta}$ for all model parameters. Warm colors indicate destabilizing effects ($S_{\lambda,\theta} > 0$), while cool colors represent stabilizing influences ($S_{\lambda,\theta} < 0$). The parameters a and q emerge as the strongest destabilizers, whereas the time-scale parameters δ, ε, and γ provide dominant damping effects.

References

[1] I. Gutman and O. E. Polansky, *Mathematical Concepts in Organic Chemistry*, Springer-Verlag, Berlin, 1986.

[2] I. R. Epstein and J. A. Pojman, *An Introduction to Nonlinear Chemical Dynamics: Oscillations, Waves, Patterns, and Chaos*, Oxford University Press, New York, 1998.

[3] P. Gray and S. K. Scott, *Chemical Oscillations and Instabilities: Non-linear Chemical Kinetics*, Oxford University Press, Oxford, 1990.

[4] S. H. Strogatz, *Nonlinear Dynamics and Chaos, Westview Press, 1994.*

[5] B. P. Belousov, A periodic reaction and its mechanism, *Collection of Abstracts on Radiation Medicine*, **147** (1959) 145–147 (in Russian).

[6] A. M. Zhabotinskii, Periodic processes of malonic acid oxidation in a liquid-phase, *Biofizika*, **9** (1964) 306–311.

[7] R. J. Field, E. Körös and R. M. Noyes, Oscillations in chemical systems. II. Thorough analysis of temporal oscillation in the bromate–cerium–malonic acid system, *J. Am. Chem. Soc.* **94** (1972) 8649–8664, https://doi.org/10.1021/ja00780a001.

[8] L. Zeng, C. Zhou, D. Wang and L. Peng, Process simplifying and analyzing of B-Z oscillating reaction, *Chemical Industry Times*, **10** (2009) 21–25.

[9] R. J. Field and R. M. Noyes, Oscillations in chemical systems. IV. Limit cycle behavior in a model of a real chemical reaction, *J. Chem. Phys.* **60** (1974) 1877–1884, https://doi.org/10.1063/1.1681288.

[10] J. R. Bamforth, J. H. Merkin, S. K. Scott, R. Tóth and V. Gáspár, Flow-distributed oscillation patterns in the Oregonator model, *Phys. Chem. Chem. Phys.* **3** (2001) 1435–1438, https://doi.org/10.1039/B010094N.

[11] P. Ruoff, pH oscillations and hysteresis in the Belousov–Zhabotinsky reaction, *J. Phys. Chem.* **93** (1989) 7394–7399.

[12] A. K. Dutt, Reversible oregonator model revisited: Thermodynamic validity, *AIP Advances*, **1** (2011) #042147, https://doi.org/10.1063/1.3664740.

[13] Z. F. Zhang and S. C. Zhang, Positively steady state and Hopf bifurcation and periodic solution of 3-D Oregonator, *Acta Math. Sinica (Chin. Ser.)* Chinese Series, **46** (2003) 167–176.

[14] S. Pippal and S. Kalsi, Solution of oregonator model by variational iteration method, *Int. J. Math. And Appl.* **11** (2023) 151–165.

[15] *D. Baleanu, K. Diethelm, E. Scalas and J. J. Trujillo*, *Fractional Calculus: Models and Numerical Methods*, World Scientific, Singapore, 2012.

[16] K. Diethelm, *The Analysis of Fractional Differential Equations*, Springer, Berlin, 2010.

[17] J. D. Meiss, Differential Dynamical Systems, *SIAM publishers, 2007.*

[18] S. H. Strogatz, *Nonlinear Dynamics and Chaos: With Applications to Physics, Biology, Chemistry, and Engineering*, CRC Press, 2008.

[19] M. Caputo, Linear models of dissipation whose Q is almost frequency independent—II. Geophysical Journal of the Royal Astronomical Society, **13** (1967) 529–539, https://doi.org/10.1111/j.1365-246X.1967.tb02303.x.

[20] A. A. Aleksandrovich Kilbas, H. M. Srivastava and J. J. Trujillo, *Theory and Applications of Fractional Differential Equations*, Elsevier, 2006.

[21] K. Diethelm, N. J. Ford and A. D. Freed, A predictor-corrector approach for the numerical solution of fractional differential equations, *Nonlinear Dynam.* **29** (2002) 3–22, https://doi.org/10.1023/A:1016592219341.

[22] E. Hairer, S. P. Norsett and G. Wanner, *Solving Ordinary Differential Equations I: Nonstiff Problems*, Springer, Berlin, 1993.

[23] R. Garrappa, Numerical solution of fractional differential equations: A survey and a software tutorial, *Mathematics*, **6** (2018) #16, https://doi.org/10.3390/math6020016.

[24] P. Rahimkhani, S. Sabermahani and H. Hassani, Physics-informed neural network method for solving delay Hilfer fractional differential equations, *Int. J. Numer. Model.: Electron. Netw. Devices Fields* **38** (2025) #e70070, https://doi.org/10.1002/jnm.70070.

[25] S. Sabermahani, P. Rahimkhani and Y. Ordokhani, Pell wavelet-optimization procedure for two classes of fractional partial differential equations with nonlocal boundary conditions, *J. Comput. Sci.* **90** (2025) #102655, https://doi.org/10.1016/j.jocs.2025.102655.